Research papers

High stability asymmetric supercapacitor cell developed with novel microwave-synthesized graphene-stabilized ruthenium antimonide nanomaterial

Precious Ekwere [*], Miranda Ndipingwi, Chinwe Ikpo, Sodiq Yussuf, Kelechi Nwambaekwe, Onyinyechi Uhuo, Emmanuel Iwuoha [*]

SensorLab (University of the Western Cape Sensor Laboratories), Chemical Sciences Building, University of the Western Cape, Bellville, 7535 Cape Town, South Africa

A B S T R A C T

Ruthenium antimony oxide (RuSbO), and ruthenium antimony oxide graphene (RuSbO-G) nanomaterial was synthesized via the microwave-assisted method for the first time and tested as a possible electrode material for an asymmetric supercapacitor device. The formation of the nanocomposites was confirmed by scanning electron microscopy (SEM) and transmission electron microscopy (TEM) images where the RuSbO material showed randomly distributed spherically shaped nanoparticles, and the RuSbO-G showed ruthenium and antimony nanoparticles scattered randomly on the graphene sheets. The SEM-electron dispersion X-ray spectroscopy (SEM-EDS) showed significant proof for nanoparticle formation with the elemental composition, while the X-ray photoelectron spectroscopy confirmed the oxidation states of the elements present. Both materials were further characterized in a three-electrode cell setup using cyclic voltammetry (CV), galvanostatic charge-discharge (GCD) and electrochemical impedance spectroscopy (EIS) and their electrochemical properties were compared to establish their suitability for energy storage purposes. From the result, different double layer properties were shown by the RuSbO and RuSbO-G in the 1 M Li_2SO_4 electrolyte. When compared to the RuSbO electrode, the composite had greater energy storage capabilities with a maximum capacitance of 289.47 F g^{-1} at 0.1 A g^{-1} current load. An efficiency of ~100 % was reached at a current density of 0.5 A g^{-1}. Subsequently, both materials were used to fabricate a portable asymmetric supercapacitor. The RuSbO-G device yielded a maximum specific capacitance of 167.96 F g^{-1}, resulting in an energy density of 75.58.0 W h kg^{-1} at a power density of 360 W kg^{-1} at 0.1 A g^{-1} current load, with ~100 % charge retention after 4900 cycles. This study turns a new research light on RuSbO based materials as an energy storage material for supercapacitors.

1. Introduction

As the world's population continues to increase, the consumption of energy also increases [1,2]. The current dependency on conventional energy sources is gradually shifting toward renewable sources. However, for this shift to transcend smoothly, energy storage systems are required to work optimally. Supercapacitors are one of those high-power devices that are being used for energy storage purposes. It has very high-power density and cycle life but relatively low energy density when compared to other storage devices. To achieve high energy density, new and advanced materials are needed to improve the capacitance of supercapacitors without compromising their characteristic high-power density and cycle life.

Carbon materials have been used as electrodes for supercapacitors for long, and the electrochemical double-layer is their main mechanism for charge storage. These materials store charges solely through the physical attraction of ions at the electrode/electrolyte interface, with no further chemical activities taking place. As a result, they have quite high charge and discharge rates, which lead to a high-power density. Nevertheless, due to their low energy density, they have not sufficiently met the need for an excellent energy storage device [3,4]. Pseudocapacitors are principally made up of metal oxides and conducting polymers, they store charges using a different mechanism known as pseudocapacitance. These are fast Faradaic reactions happening at the electrode surface of metal oxides or conducting polymer [5]. Currently, pseudocapacitance materials are being researched as alternative

electrode materials. However, they offer enhanced energy density at the cost of cyclic stability and power density which characterizes an ideal supercapacitor [6]. So far, an intense effort has been made to improve traditional materials such as carbon materials, transition metal-based materials and conducting polymers. Ruthenium oxide has been one of the most widely researched transition metal-based materials because of its theoretical high capacitance [7–9]. However, RuO_2 is very expensive and in addition to cost, it also exhibits poor cycling. For example, hydrous ruthenium oxide electrodes were effectively arranged by electrophoretic deposition by Jang et al. [10], and the material was heat-treated to control the water content at 150 °C, 250 °C and 300 °C. The anode conveyed a huge explicit capacitance (734 F g^{-1} and 608 F g^{-1} at an output pace of 1 mV s^{-1} and 50 mV s^{-1} sweep rates respectively) but lacked cyclic stability as just 4 % of the underlying capacitance was retained after 50 cycles. In recent times, novel materials of ruthenium based composites have been synthesized and proposed to be capacitive [11–13]. Aside from the low cyclability of RuO_2, the compound is additionally prevented by; the re-stacking of its particles, and low conductivity between nanoparticles, therefore, the actual test of the Cs are normally lower than the calculated value. The production of hybrid electrodes that combine RuO_2 with relatively high surface area carbon materials is a matter of great consideration to avoid these drawbacks. Surktha et al. [14] synthesized a composite of RuO_2 with pre-nitrogen-doped reduced graphene oxide aerogel (NGA), the electrode material had a 79.6 F g^{-1} capacitance and a 64 u W cm^2 PD with 16.3 μg mass of active material. The electrode maintained 100 % stability for about 200 cycles. The capacitance of NGA alone was also calculated and was lower than that of the composite which shows the contribution from the RuO_2. Different ruthenium-based material has been explored, for instance, compounds of ruthenium like its nitrides [15–17] sulphides [18–20], and even tellurides [18] have been explored. However, until date, its antimonide counterpart has never been investigated.

Antimony based compounds that are gradually gaining popularity in sodium/lithium (Na/Li) ion batteries as efficient anode materials have a theoretical capacity of up to 660 mAh g^{-1} [21–23]. Its compounds have been tried for supercapacitor applications severally, copper antimony sulphide (Cu_3SbS_4) was successfully synthesized by Mariapan et al. and yielded a capacitance of up to 60 F g^{-1} at 5 mV s^{-1} resulting in an energy density of 11.373 W h kg^{-1} at a power density of 175 W kg^{-1} and good capacitance retention after 2500 cycles [21]. Korkmaz et al. [24] reported thin films of graphene oxide/antimony sulphide (on Si substrate) generated at various deposition temperatures using a chemical bath deposition method and their supercapacitor properties. Their specific capacitance values at 5 mV s^{-1} were 562 F g^{-1} between the −0.2 V to 0.8 V range. Lin et al. [25] synthesized a micro spindle hierarchical structure of antimony phosphate, following a facile solvothermal route. The electrochemical micro spindle antimony phosphate ($SbPO_4$-Ms) was compared with nanoparticles of antimony phosphate ($SbPO_4$-Np). The reversible redox transition between Sb^{3+} and Sb metal states provides pseudocapacitance and makes this material suitable for energy storage. More so, the Sb-O-P bond of PO_4^{3-} provides stability to the Sb^{3+} by creating an Sb-O-P bond inductive effect. The $SbPO_4$-Ms showed a higher electrochemical capacitance than the nanoparticle antimony phosphate. Its capacitance was 234.23 F g^{-1} at 0.5 A g^{-1} and 43.88 F g^{-1} at 10 A g^{-1} while that of the latter was 3.44 and 142.10 F g^{-1} at 0.5 and 10 A g^{-1} current density respectively. The $SbPO_4$-Ms was also more stable with 90% capacitance retention as compared to $SbPO_4$ Np which only exhibited 59 % capacitance retention.

The major drawback for antimony is the resultant effect of its volume expansion which results in reduced stability. However, the use of carbon material such as graphene has been found to provide stability, by acting like a mechanical buffer that will reduce the volume change while facilitating electron transport during the charge-discharge process [22]. Several methods have been employed to decrease volume expansion, including (1) the production of metallic alloys, (2) the formation of a stable heterostructure oxide (e.g., Sb/S_2bO_3), and (3) nanoscale

tailoring and anchoring in a carbon matrix.

In this report, a new energy storage material based on a binary metal oxide composite stabilized with graphene is presented. Ruthenium antimony oxide-graphene nanocomposite (RuSbO-G) was synthesized via microwave-assisted (MW) method. First graphene oxide was synthesized from graphite powder using the Hummers method, then the pristine RuSbO compound and the RuSbO-G nanocomposites were synthesized via MW synthesis. The materials were thoroughly characterized morphologically, spectroscopically, and electrochemically. The RuSbO and RuSbO-G electrodes demonstrated a very capacitive energy storage mechanism, with CV curves that match the behaviour of typical pseudocapacitance materials. The materials were used as an electrode for an asymmetric supercapacitor device and a capacitance of 167.96 F g^{-1}, which translated into an energy density of 75.58 W h kg^{-1} at a power density of 360 W kg^{-1} and at 0.2 A g^{-1} current load was recorded for the graphinised composite.

2. Experimental

2.1. Materials

Microcrystalline graphite (2-15 μm, 99.99 %) was purchased from Alfar Aesar (Kandel, Germany) Nickel foam (1.6 mm thick, 0.25 μm pore diameter) was purchased from MTI Corporation, (Richmond, California, USA). Hydrogen peroxide solution (30 wt% in water, American chemical society (ACS) reagent), concentrated hydrochloric acid (reagent grade and assay 36.5–38.0 %), sodium borohydride (98.0 %), potassium permanganate (≥99.0 %, ACS reagent), concentrated sulphuric acid (99.99 %), Ruthenium (111) chloride hydrate (99.98 % trace metal bases), antimony pentoxide (99.99 % trace metal bases), polytetrafluoroethylene (mean particle size 20 μm), activated charcoal (Norit ® pallets), anhydrous *N*-methyl-2-pyrrolidone (99.50 %) and carbon black (4 μm mesoporous carbon matrix, ≥99.95 % metal bases), ethylene glycol (EG) (99.80%), ethanol (absolute, ≥99.80%) were purchased from Sigma-Aldrich (St Louis, Missouri, USA) and were all used without further purification.

2.2. Microwave-assisted synthesis of RuSbO and RuSbO-G nanocomposite

The MW-assisted synthesis of RuSbO was carried out using an Anton Parr multi-wave Pro microwave system. It is equipped with an IR temperature sensor that controls the temperature during the process. $RuCl_3$·xH_2O (1 mmol) and 2 mmol of $SbCl_5$ was added to 30 mL of ethylene glycol with continuous stirring for 0.5 h. $NaBH_4$ (1.5 g) was slowly added to the above-mixed solution, sonicated for 10 min and allowed to cool. The resultant mixture was MW-irradiated at 190°C for 10 min. The resulting products were separated by centrifuging, washed with deionized water and dried at 60 °C under vacuum for 12 h.

One hundred milligrams of GO synthesized using Hummers method, is dissolved in 30 mL of ethylene glycol and sonicated for 2 h to form a homogenous dispersion. $RuCl_3$·xH_2O (1 mmol) and 2 mmol of $SbCl_5$ were added to the dispersed solution and sonicated for 0.5 h. $NaBH_4$ (2 g) was slowly added to the above mixture, which was sonicated for 10 min and transferred to a microwave vessel. The resultant mixture was MW-irradiated at 190 °C for 10 min. The resulting products were separated by centrifuging, washed with deionized water, and dried at 60 °C under vacuum for 12 h.

2.3. Material characterization

The elemental and morphological composition of the nanoparticles were obtained using a Carl ZEISS ULTRA scanning electron microscope GmbH (Jena, Germany) fitted with an energy dispersion spectrometer and a FEI Tecnai G2 F@ X-T win MAT 200 kV Auriga field emission electron microscope (Eindhoven, Netherlands). All analysis was
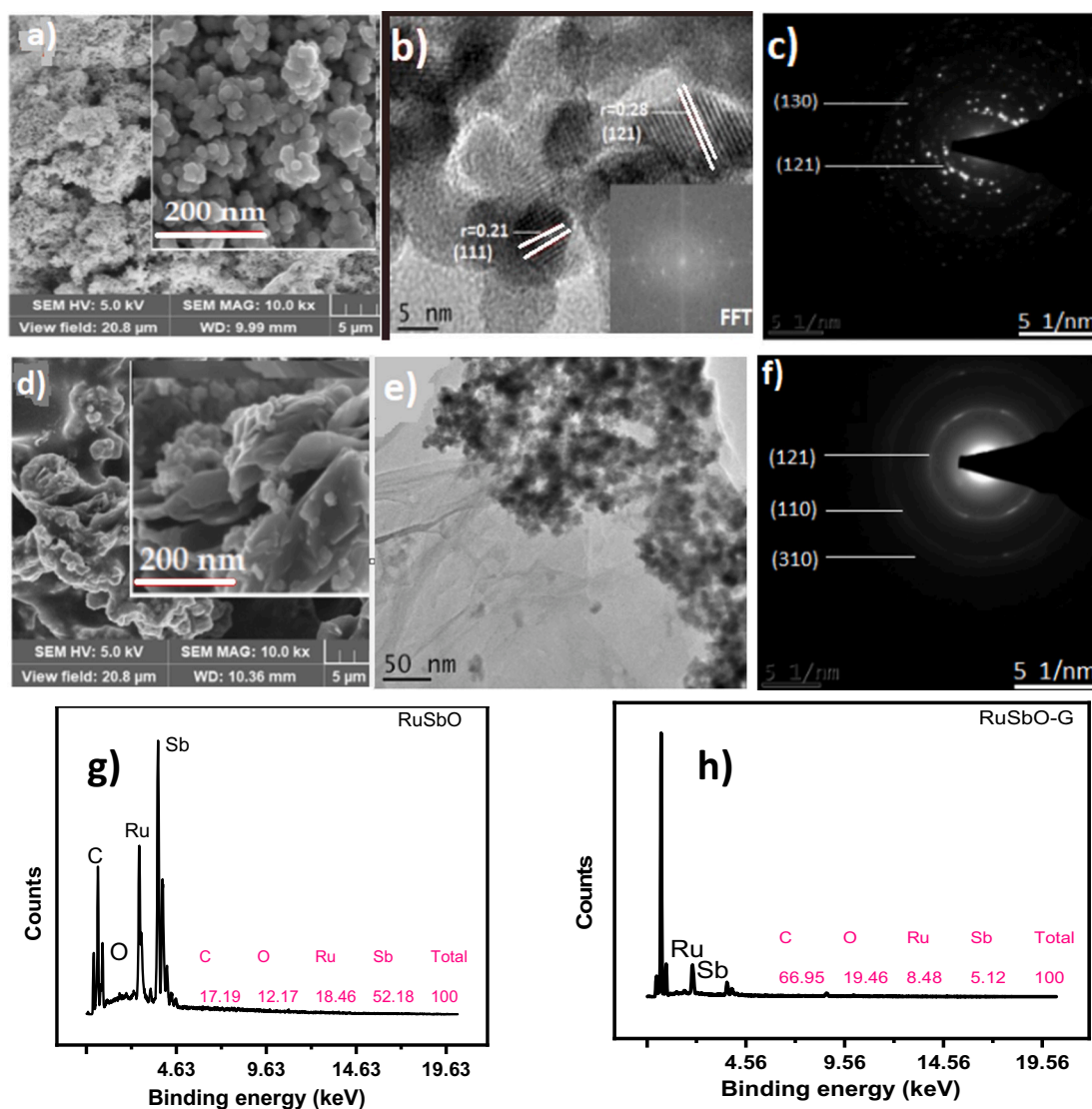
Fig. 1. RuSbO: a) SEM image, b) TEM image showing the lattice fringes (the inset is the FFT), c) SAED pattern, g) EDS spectrum (the inset is the percentage elemental composition) and RuSbO-G: d) SEM image, e) TEM image showing the graphene sheet f) SAED pattern, h) EDS spectrum (the inset is the percentage elemental composition).

performed on a nickel-copper grid. The samples for TEM characterization were drop-coated into the Cu TEM grids and scanned in high-resolution transmission electron microscopy (HR-TEM) with an FEI Technai G20 F20X-Twin MAT 200 kV Field Emission Transmission Electron Microscope (Eindhoven, Netherlands) equipped with both EDS and selected area electron diffraction (SAED). The X-ray powder diffraction (XRD) pattern was obtained for all the nanoparticles with a D8 advance multipurpose X-ray diffractometer (BRUCKER-AXS, Berlin, Germany) using copper kα1 radiation ($\lambda \sim 0.154$ nm) operating at 40 kV and 40 mA. XRD patterns were collected from 15 to 70 (2q) with step size of 0.034° in 2q. The functional group present in the sample was determined using a Perkin Elmer Spectrum 100 series Attenuated Total Reflectance (ATR) Fourier Transform Infra-red spectrometer with 4 cm^{-1} resolutions (Perkin-Elmer, Boston, MA, USA). The nanoparticles Raman spectra were obtained using an Xplora Olympus BX41 Raman Spectrometer (Horiba, Tokyo, Japan) using a 532 nm laser as the excitation source. Optical absorption spectra were acquired from ethanolic dispersions of the nanocrystals at room temperature using a Varian Cary 300 UV–Vis-NIR spectrophotometer (Agilent, Santa Clara, CA, USA). At room temperature, infrared spectroscopic investigations between 4000 and 400 cm^{-1} were carried out. The powdered nanocrystals were

deposited on a diamond disc, and infrared spectra were acquired using an Attenuated Total Reflectance/Perkin-Elmer Spectrum 100 Series Fourier Transform Infrared (FTIR) Spectrometer (Perkin-Elmer, Boston, MA, USA). The photoluminescence properties were obtained from NanoLog HORIBA using the software FluorEssence V3.9. (Johannesburg, South Africa). All electrochemical studies were performed on a VMP-300 potentiostat from the Bio-Logic SAS instrument (France).

2.4. Electrode preparation and electrochemical measurements

To prepare the working electrode, the active material; RuSbO and RuSbO-G (70 %), a conducting agent; carbon black (20 %) and a binder; polytetrafluoroethylene (10 %) was mixed in a mortar and crushed to fine powder. Then 3 drops of anhydrous *N*-methyl-2-pyrrolidone were added and mixed to form a uniform slurry. Nickel foam was cut into rectangular shapes of 0.5×1 cm^2 and coined shapes of 20 mm in diameter. The foams were cleaned to remove all surface oxide layers in 1 M HCL solution, absolute ethanol, and deionized water respectively, with ultra-sonication for 15 min in each solvent, and dried at $90°C$ for 12 h. The homogenous paste was coated on 0.5 cm^2 diameter of the nickel foam and dried at 80 °C for 12 h. In a three-electrode cell setup,
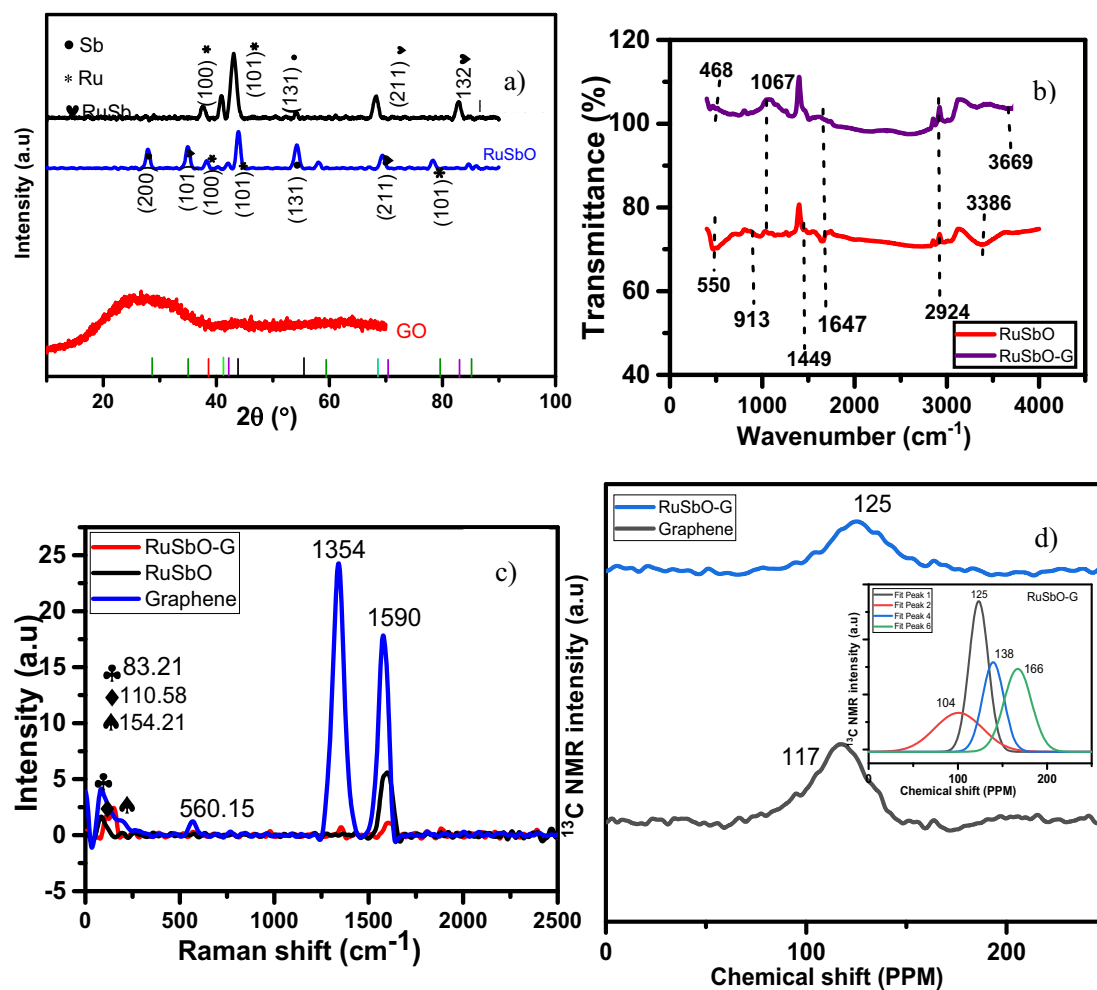
Fig. 2. RuSbO and RuSbO-G overlayed on graphene a) XRD analysis showing the change of intensity and peak position of the crystal phases b) FTIR spectra c) Raman spectra d) NMR spectra of graphene and RuSbO-G. (The inset is the deconvoluted 126 ppm peak of RuSbO-G.)

Ag/AgCl and Pt wire were used as the reference and counter electrode respectively. While for the full cell, the paste was coated into the coin-shaped nickel foam and assembled in a Swagelok with activated carbon as the negative electrode. The cyclic voltammograms were recorded between −0 to 0.6 V potential window at different scan rates. The electrochemical impedance measurements were obtained at a frequency range of 0.1 MHz to 100 MHz with 10 points per decades, and the galvanostatic charge-discharge profiles were measured at different current densities at a mass loading of 4 mg (RuSbO) and 3.9 mg (RuSbO-G). All electrochemical characterization of material was done in the three-electrode cell using 1 M Li_2SO_4, electrolyte, and the device was tested at 1.8 V in 1 M Li_2SO_4.

3. Result and discussion

3.1. Morphological studies

3.1.1. SEM and TEM analysis

SEM was used to investigate the surface morphology, average particle size and shape of the nanoparticles. The SEM image for the pristine RuSbO Fig. 1a revealed clustered spherically shaped particles that ranges between 10 nm and 40 nm, while those of RuSbO-G (Fig. 1d) was more dispersed on the graphene layer with sizes ranging from 8 nm to 35 nm. The TEM result (Fig. 1b, e) confirms that while the RuSbO was severely agglomerated, the RuSbO-G was more dispersed. Therefore, the graphene must have acted as a dispersing agent and the metal oxides, as

a spacer for the graphene sheets [23]. The more dispersed material is expected to provide more intercalation sites for electrolytes ions, resulting in higher electrochemical performance [26]. The more dispersed composite material will also have an improved surface area and several accessible pores for the electrolyte thus increasing ion mobility. Therefore, the addition of graphene showed a better structural property [27]. The RuSbO-G particles have a diameter between 9 nm–25 nm from the TEM data. The particles are better distributed in the composite as seen in the TEM image than in the RuSbO. This will give rise to better packing porosity and geometrical tortuosity thereby having better pathways for the electrolyte ions [28,29]. The fast Fourier transform (FFT) image (Fig. 1b inset) was obtained from the lattice fringes of the RuSbO TEM monogram and was used to confirm the d-spacing and possible phases of the particles obtained from XRD data. By analyzing the TEM image, the lattice fringes are shown to be 0.28 nm and 0.21 nm in the RuSbO and it is along the (121) and (111) plane. For the RuSbO-G the lattice fringes were not obvious. This is due to the incorporation of amorphous graphene into its structure. The selected area electron diffraction (SAED) pattern (Fig. 1c, f) shows that the composite is crystalline in the (130), (121) direction for the RuSbO compound and in the (121), (110), (310) direction of the RuSbO-G nanocomposite. This is also confirmed by the data from the XRD analysis.

Table 1
Functional groups and vibrational bands of RuSbO and RuSbO-G.

Functional group/bands	Material/wavenumber (cm^{-1})	
	RuSbO	RuSbO-G
O-H	3386	3781
C-H		288
C=C		2041
C=O		1800
C-O		1510
Sb-O	650	550
Ru-O	455	459

3.2. Spectroscopical studies

3.2.1. Energy-dispersive X-ray spectroscopy (EDS)

EDS from the SEM analysis was used to ascertain the elemental composition of RuSbO and RuSbO-G. The EDS analysis confirms the presence of Ru, Sb and O in RuSbO and Ru, Sb, O and C in RuSbO-G was also confirmed (Fig. 1g, h). The EDS data reveals that Sb was in a high quantity in the pristine material than in the composite, this could mean that the presence of graphene inhibited the nucleation/growth of Sb nanoparticles. The data in the inset reflect the weight percent of each element; the data reveals that a substantial amount of graphene was in the composite; this will increase the composite's stability and limit the volume expansion of Sb and Ru.

3.2.2. X-ray diffraction (XRD)

Fig. 2a shows the XRD pattern of the RuSbO and RuSbO-G materials. Samples were observed as Ru, RuO$_2$, and Sb$_2$O$_4$. All the diffraction peaks are indexed to base-centered orthorhombic Sb$_2$O$_4$ according to the Joint committee on powder diffraction standards. (JCPDs card No _2 37 08 54) with lattice parameter a = 6.50900 Å, b = 6.51200 Å, c = 3.08300 Å and tetragonal RuO$_2$ (JCPD card No 2_43-1027) with lattice parameter a = 4.4994 Å and c = 3.10710 Å. The sample shows a diffraction peak at 2θ = 27.83°, 34.8°, 44.02°, 53.1°, 69.17° which belongs to the (200), (101), (100), (131), (211) phase of RuO$_2$, and Sb$_2$O$_4$. The most intensive peak at 44.0° shifted to 43.83° for the RuSbO-G XRD graph [30,31]. This is suspected to be due to the incorporation of ruthenium in the antimony lattice. The XRD analysis was also used to quantify the difference in interlayer spacing arising from the attachment of graphene to the RuSbO nanocomposite. A clear shift in the peak to an increase of 0.4 nm in the spacing between the layers indicates that the addition of graphene can effectively expand the interlayer spacing of the composite, which will facilitate the diffusion and transport of electrolyte ions during the charge/discharge process [32]. The composite, RuSbO-G showed diffraction peaks at 2θ = 37.55°, 40.99°, 43.09°, 55.3°, 68.4°, 83.08° belonging to (100), (131), (211) phases. With the addition of graphene two characteristics peaks at 2θ = 27.83° and 34.88° belonging to the (200) and (101) phase of RuO$_2$ and Sb$_2$O$_4$ significantly reduced, indicating that the structure of the material changed with the addition of graphene. The increase in intensity and shift in the position of the peaks in RuSbO-G compared to those of RuSbO is an indication of a structural change, owing to the addition of graphene. Crystal size was also estimated using the Debye-Scherer formula for the most intense peaks in the XRD patterns. The size was an average of 37.30 nm in the pristine material and 36.33 nm in the composite material. The difference in diameter is due to the incorporation of graphene and it is confirmed in the SEM and TEM analysis.

3.2.3. Fourier transform infra-red spectroscopy (FTIR)

The FTIR absorption spectra of RuSbO and RuSbO-G in the 4000–400 cm^{-1} region is shown in Fig. 2b. The FTIR analysis was carried out to determine the presence of bonding or stretching vibrations in the synthesized RuSbO and RuSbO-G. The distinctive OH stretch is confirmed by the broadband at 3386 and 3669 cm^{-1} in the RuSbO and

RuSbO-G spectrum respectively. The vibration of molecular water's hydroxyl groups and the stretching vibration of the peroxo group induce the absorption band around 2924, 1647, 1449 and 1067 cm^{-1}. The vibrational band at 981 and 468 cm^{-1} is characterized by the presence of the asymmetric stretch of Ru—O [33]. The Sb—O stretching is visible in the RuSbO spectrum at 550 cm^{-1} [34]. The metal-oxygen stretching absorption recorded in 550 cm^{-1} and 469 cm^{-1} for SbO and RuO is stronger in RuSbO. The shift in band position and intensity in the RuSbO compared to RuSbO-G indicates the creation of new structural material. Table 1 shows all the distinct functional groups present in RuSbO and RuSbO-G.

3.2.4. Raman spectroscopy

The Raman spectroscopy of RuSbO and RuSbO-G was carried out to further establish the structural properties of RuSbO and RuSbO-G material. The technique has established itself as the most basic and non-destructive method for analyzing carbon and carbon-based structures. Fig. 2c displays the D and G bands that characterize carbon compounds in the Raman spectra of graphene. The G-band is produced by in-plane SP^2 C—C stretching and can be found in all carbon structures, whereas the D-band is produced by flaws and edges in the carbon grid [35,36]. The intensity ratio of the D and G bands (ID/IG) is an indirect measure of the material's disorder. The D and G bands can be found at 1354 and 1590 cm^{-1} respectively. From the spectrum, the characteristics of Ru—O peaks can be identified at the 154.21 cm^{-1} position. The bands at (110.58 cm^{-1}) and (153.2 cm^{-1}) belong to the Eg and A1g vibrational modes of Sb—O [37,38], while the band around 560.15 cm^{-1} is related to Sb$_2$O$_4$. In the composite's material, the peaks belonging to RuO and SbO are present alongside the peaks belonging to carbon.

3.2.5. Solid-state nuclear magnetic resonance spectroscopy (NMR)

The NMR spectra of RuSbO-G and graphene are shown in Fig. 2d. Pure graphene's carbon environment was compared to that of RuSbO-G samples. The prominent peak at 117 ppm, which belongs to graphitic sp^2 carbon as seen in graphene, shifted to 125 ppm, while a shoulder peak can be seen at 104 ppm and at 166 ppm. Other shoulder peaks can be seen at 92 and 138 ppm. The inset shows the graph of the deconvoluted peaks showing that the chemical environment of carbon is different from those of graphene and RuSbO-G. The FWHM of the most intense peak of graphene and RuSbO-G samples are 31 and 25 ppm [39,40].

3.2.6. X-ray photoelectron spectroscopy (XPS)

XPS technique was used to determine the oxidation states and stoichiometry of RuSbO-G.In Fig. 3a, the elements Ru, Sb, C and O were detected in the RuSbO-G nanomaterial. The high-resolution Ru 3d + C1s scan of RuSbO-G (Fig. 3b) was split into six peaks at 289.3, 287.3, 285.8, 285.3, 284.5 and 280.1 eV. This indicates the presence of carbon-oxygen components (O-C=O, C=O, C—O,) sp^2 hybridized carbon (C—C) and Ru/RuO$_2$ as seen in the FTIR analysis [41,42]. The high-resolution Sp3 d3 + O1s spectrum of the composite (Fig. 3c) was split into four main peaks at 539.9, 537.6, 530.7 and 528.6 eV. Which belonged to Sb$_3$O$_5$/Sb$_3$O$_3$, Sb$_3$d$_3$, C=O, C—O and Sb [43]. The MW synthesis successfully introduced antimony and ruthenium atoms into the graphene matrix.

3.2.7. Photoluminescence spectroscopy

To investigate the photo-excited electron transfer in RuSbO and RuSbO-G composites, the photoluminescence spectra (PL) were obtained. Fig. 3d depicts the PL emission spectra of RuSbO and RuSbO-G hybrids. The dispersed sample in ethanol solution was measured at room temperature and was excited at 235 nm. In the RuSbO, a near band edge emission peak at 383 nm and a broad shoulder at the low energy side (456) was observed which arise from the MLCT excited-state emission [44]. The intensity of the PL peak of RuSbO is lower than that of RuSbO-G. It may be noted that the introduction of graphene reduced the agglomeration of the RuSbO samples as seen in the TEM and SEM images. These may also have generally reduced surface defects and
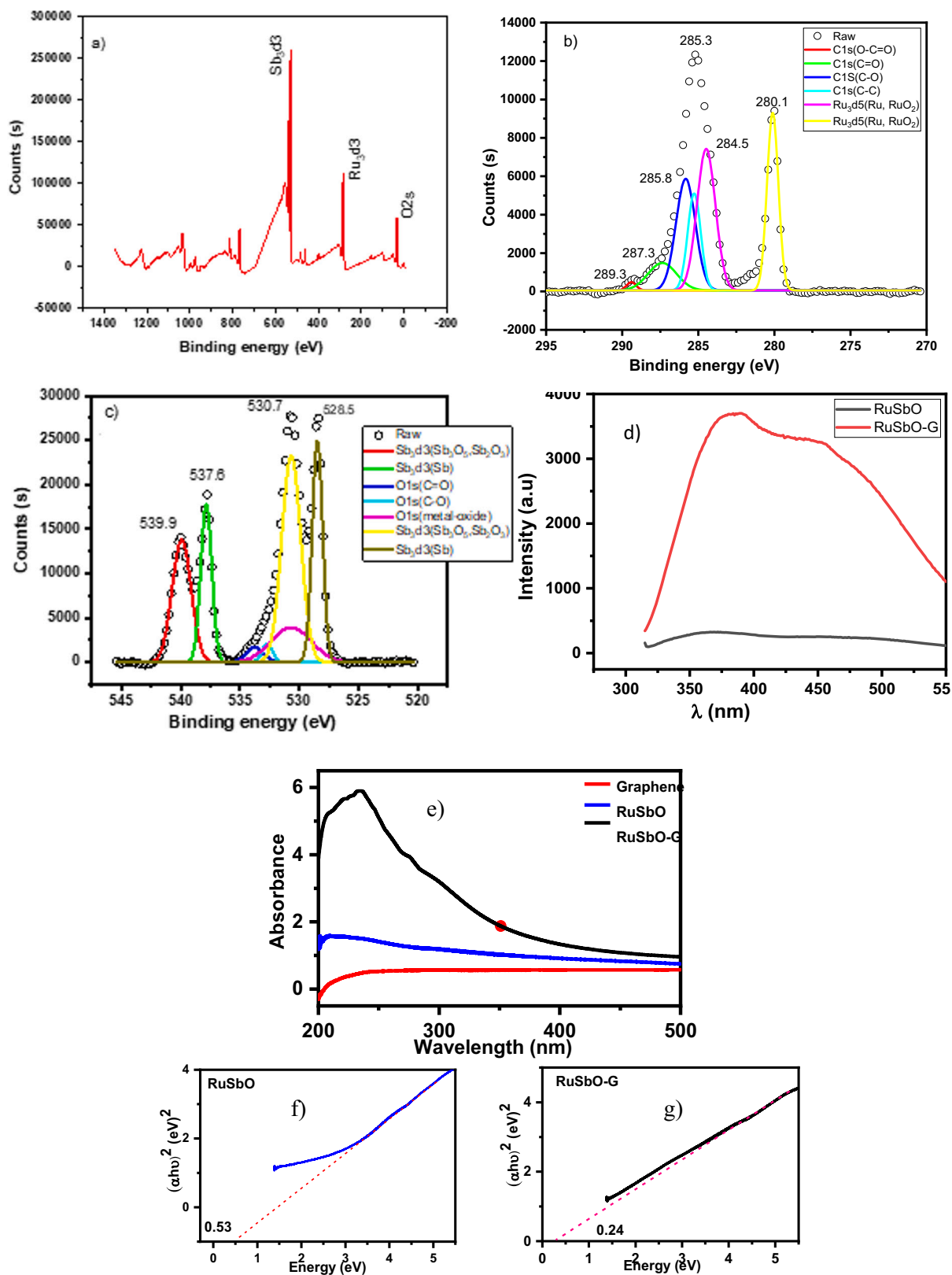
Fig. 3. XPS spectra of; a) RuSbO-G, b) Ru 3d + C1s, c) Sb 3d + O1s b), d) the PL emission spectra of RuSbO and RuSbO-G, e) the UV–vis spectra of RuSbO and RuSbO-G overlayed on graphene and f & g is their corresponding Tauc plots.
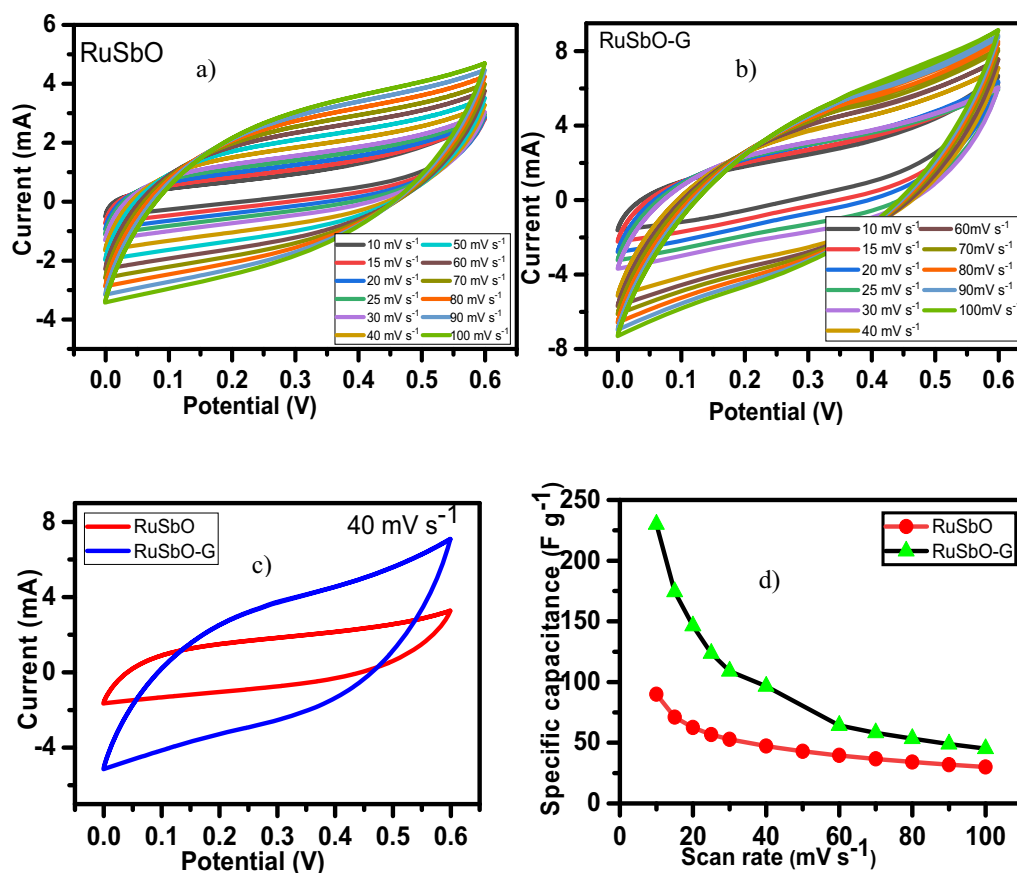
Fig. 4. RuSbO and RuSbO-G: a & b) CV plots at different scan rates, C) CV plots comparing their voltammograms at 40 mV s^{-1} scan rate, d) is their specific capacitance at different scan rate. All analysis was done in 1 M Li$_2$SO$_4$ electrolyte.

decreased the number of trap sites in the system [45]. On the other hand, the agglomeration in RuSbO must have introduced lattice strain, caused contraction of lattice parameter, and given rise to defects and vacancies in the system. All these together can initiate indirect transitions in the system, thus reducing the PL intensity [46]. A sample's particle size and morphological characteristics have a substantial influence on its bandgap energy, which is also essential in defining its electrochemical activity. The bandgaps of the samples can be calculated from the PL wavelengths using.

$$E = hC\lambda \tag{1}$$

where h is the Planck constant; c is the velocity of light, and λ is the wavelength of the absorption peak [47]. The bandgap for RuSbO was 3.48 eV while that of RuSbO-G was 3.18 eV. The reduced bandgap in the composite will facilitate the transfer of charge. Therefore RuSbO-G is expected to have a better electrochemical performance.

3.2.8. UV–vis spectroscopy

The presence of Ru and Sb nanoparticles is confirmed by the UV–Vis absorption test. When compared to pristine graphene, all RuSbO nanoparticles have apparent exponential decay curves in the 200–400 nm region, which could be attributable to Mie scattering (Fig. 3c) [48,49]. This indicates the stability of RuSbO nanoparticles as well as their good solvent dispersion [50]. With the addition of graphene, the curve exhibits a more evident exponential decay, indicating that the RuSbO-G nanoparticles have increased dispersion capacities. The bandgaps of RuSbO and RuSbO-G were estimated to be 0.60 and 0.23 eV, respectively, using the Taucs plot from the origin program (Fig. 3f, g) [51]. When compared to RuSbO nanoparticles, the bandgap of RuSbO-G composite is smaller due to the effect of carbon [52,53]. The smaller

conduction band indicates that the synergy between Ru, Sb and C can facilitate the transmission of charges, which will induce high power density. The small band gap value of this material might be owing to their high crystallinity [54,55].

3.3. Electrochemical studies

3.3.1. Cyclic voltammetry

The electrochemical performance of the pristine and composite material was investigated by cyclic voltammetry (CV), galvanostatic charge-discharge (GCD) and electrochemical impedance spectroscopy (EIS) measurement with 1 M Li$_2$SO$_4$ as the electrolyte. In the half cell, otherwise called the three-electrode system, CVs were run at scan rates ranging from 10 mV s^{-1} to 100 mV s^{-1} at a potential window of 0.0 V to 0.6 V (Fig. 4a, b). At a low scan rate, the CV curves of both samples were virtually rectangular, and no redox peak was seen. This indicates that the materials had nearly perfect capacitive behaviour. The capacitive current increases as the scan rate increases and the shape of the CV plots gradually changes from rectangular to oval, due to the internal resistance of the electrode. Which may be due to the limited charge accumulation and low conductivity of Li$_2$SO$_4$ aqueous solution, as well as the diffusion limits of Li$^+$ and SO$_4^{-2}$ ions in the electrodes [56,57]. As the voltage scan rate increased, the deviation of the voltammogram from the ideal rectangular structure also increased. This can be because of the electrochemical polarization of the electrode with the graphenised material showing a higher degree of polarization. The oxygen groups at the edges of the graphene nanosheet as seen in the FTIR are responsible for the pseudocapacitance contribution and the electrochemical polarization of the electrode [58,59]. Increasing the scan rate limited the reaction site thus exonerating the contribution of the inner sites [60]. In

Table 2
The capacitance of RuSbO and RuSbO-G at different scan rates.

Scan rates	Capacitance (F g^{-1})	
	RuSbO	RuSbO-G
10	43.9	109.53
15	34.69	83.07
20	30.49	69.64
25	27.64	58.9
30	25.75	51.89
40	23.07	45.95
60	19.31	30.63
70	17.89	27.73
80	16.67	25.44
90	15.58	23.29
100	14.63	21.49

Fig. 4c, the C*V* plots of RuSbO-G and RuSbO are compared at 40 mV s^{-1} and the C*V* plot of RuSbO-G has a higher current response than the C*V* plot of RuSbO. It also showed a larger charge buildup area and thus a higher capacitance than the CV plot of RuSbO. This is due to the incorporation of graphene into the material, which results in a superior surface for charge buildup. From the plots the RuSbO-G composite performed better than the pristine material. This is because; 1) combining two metal structures creates an open micro/nano-architecture with more contact sites and optimizes electrochemical activity in the contact site. Which results in a synergistic impact in the electrochemical performance [61,62]. 2) Addition of graphene must have increased the conductivity of the material, by providing better surface area and a quicker diffusion pathway [63]. The specific capacitance of the three materials was calculated from the equation below:

$$C_{sp} = \frac{1}{2m\nu\triangle V} \int_{-v}^{+v} I dv \tag{2}$$

where m is the active mass of the electrode (g), ν is the scan rate (V s^{-1}), $\triangle$V is the potential window in (V) and $\int_{-v}^{+v} I dv$ is the charge obtained from the integrated area of the voltammogram. RuSbO-G showed a better electrochemical performance with a high specific capacitance of 109.53 F g^{-1} at 10 mV s^{-1} and up to 21.19 F g^{-1} at 100 mV s^{-1}. While for RuSbO the values were 43.9 F g^{-1} at 10 mV s^{-1} to 14.63 F g^{-1} at 100 mV s^{-1}. The specific capacitance values are plotted against potential sweep rates as shown in Fig. 4d. When the voltage scan rate was raised, the specific capacitance values for both materials decreased gradually. The drop in capacitance value as the scan rate increases is a frequent phenomenon caused by insufficient time for electrolyte ion diffusion, and charge storage is limited to the outer surface area only [64]. From the plot, the RuSbO-G can be seen to have the highest specific capacitance with a slow decrease at higher scans, thus showing its high-rate capability. The better performance of RuSbO-G across all scan rates is mostly owing to the integration of graphene into the RuSbO matrix, thus improving the morphology for better charge storage and stability [65]. The specific capacitance of RuSbO and RuSbO-G across all scan rates is represented in Table 2.

3.3.2. Galvanostatic charge-discharge

The performance of RuSbO and RuSbO-G electrodes was investigated at current densities of 0.1 0.2, 0.4, 0.6, 0.8, 1, and 2 A g^{-1} (Fig. 5a, b). The RuSbO-G electrode's GCD curves show a high specific capacitance when compared to RuSbO. The presence of near triangular curves, confirms the electric double layer capacitive charge storage mechanism occurring at the electrode/electrolyte interface [66]. The GCD curves are almost symmetrical, with only a minimal voltage drop caused by the equivalent series resistance (ESR). The charge and discharge processes have matching duration, indicating a high Coulombic efficiency and electrochemical reversibility [65]. These observations are consistent with the oxidation and reduction profiles reported in the C*V* curves. The
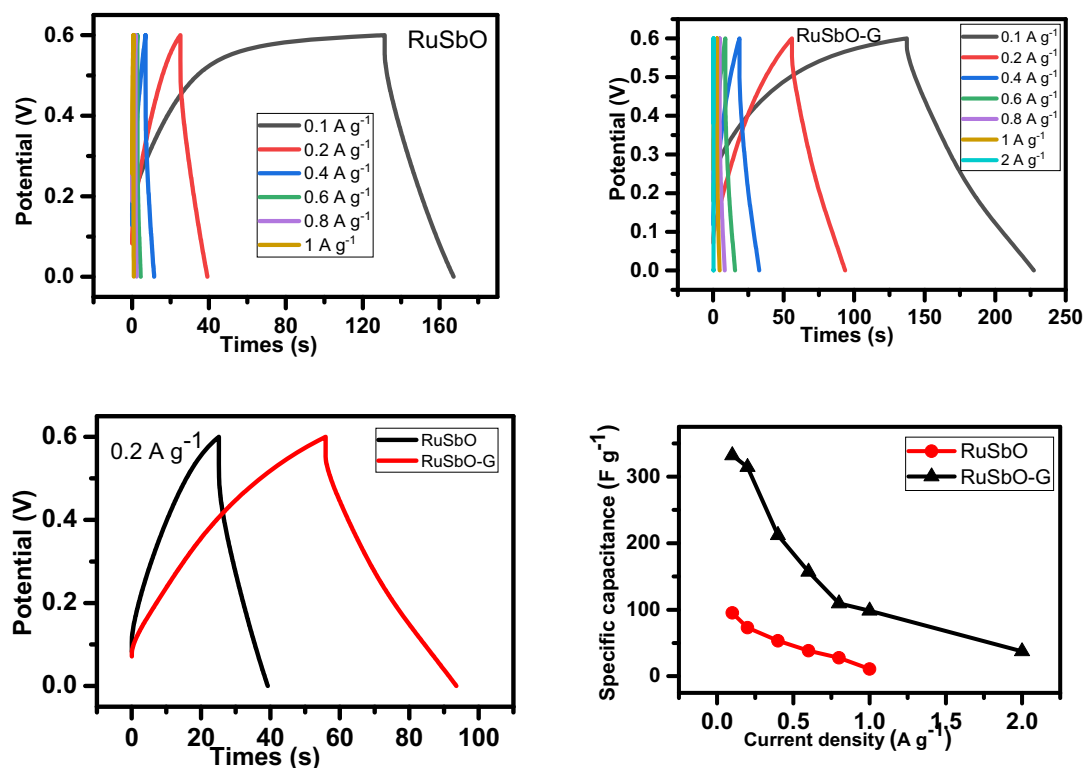

Fig. 5. RuSbO and RuSbO-G: a & b) GCD plots at different current densities, C) GCD plots comparing their charge and discharge profile at 0.2 A g^{-1} current density, d) is their specific capacitance at different current density. All analysis was done in 1 M Li$_2$SO$_4$ electrolyte.
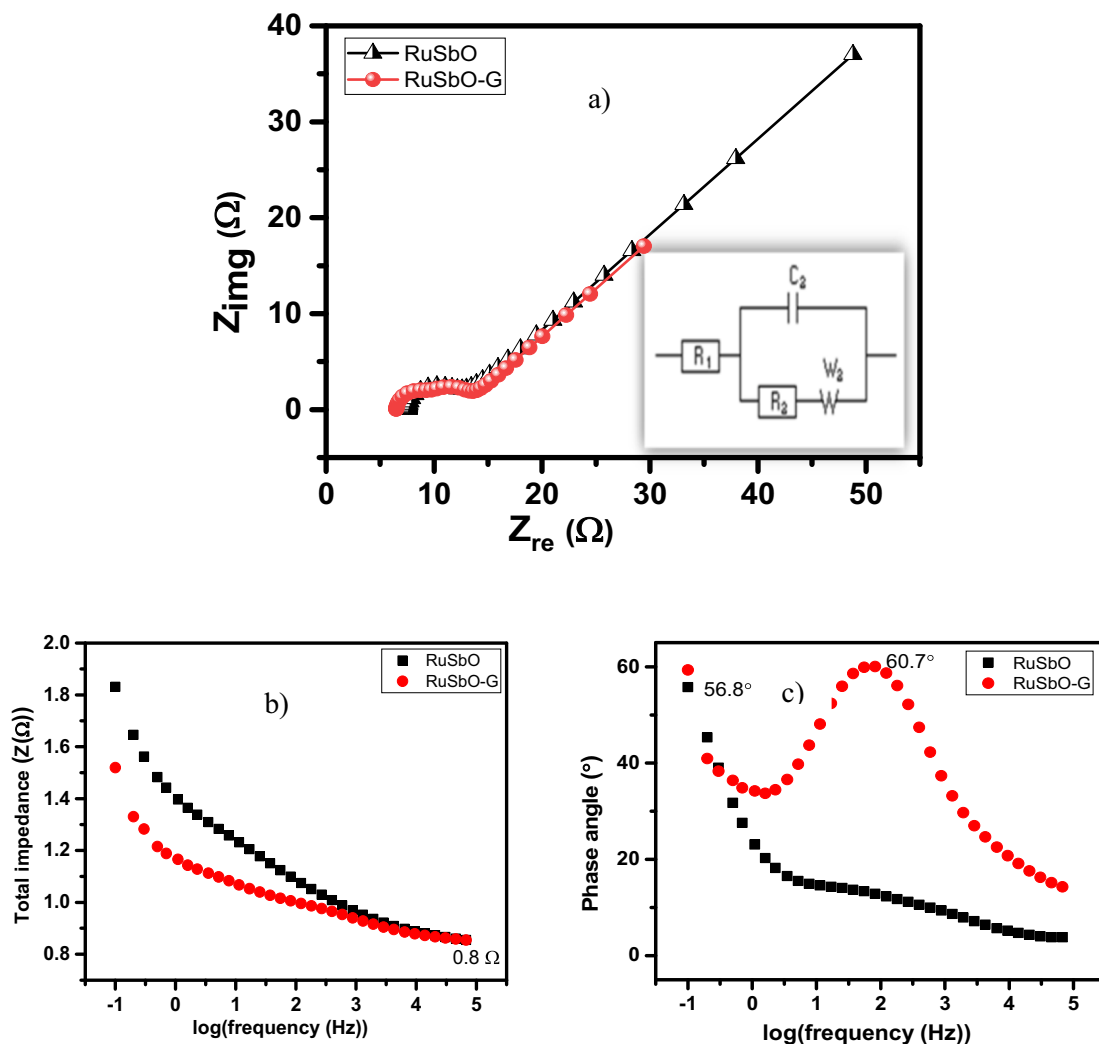
Fig. 6. Nyquist plot of RuSbO and RuSbO-G, the inset is the equivalent circuit, b) bode plots of RuSbO and RuSbO-G, c) total impedance plots of RuSbO and RuSbO-G.

specific capacitance (C) was determined using the equation.

$$C_s = \frac{I \times t}{m \times V - IR_{drop}}$$

(3)

where I is the constant current, m is the active material mass, and t is the discharge time corresponding to the voltage change V [22]. The RuSbO-G electrode has the highest specific capacitance at the same current density when compared to RuSbO. The highest capacitance of the RuSbO-G electrode, for example, reached up to 289.47 F g^{-1} at 0.1 A g^{-1}, while RuSbO was 95.33 F g^{-1}. This is due to graphene's porous microstructure, which facilitates electrolyte infiltration and contributes to the development of electric double-layer capacitance. Fig. 5c shows a comparison of the rate capabilities of RuSbO-G and RuSbO electrodes at various current densities. At a current density of 0.2 A g^{-1}, RuSbO-G has a specific capacitance of 236.07 F g^{-1}, which is substantially higher than that of RuSbO (73.07 F g^{-1}). Notably, as the current density increased to 1 A g^{-1}, the RuSbO-G maintained a high capacitance of 74.05 F g^{-1}, retaining 30 % of its capacitance. RuSbO electrodes, on the other hand, exhibit poorer capacitance retention of 10 %, indicating that the structure of the RuSbO-G improved electrolyte ion diffusion. The specific capacitance decreases as the current increases. The drop in specific capacitance values was noticeable in the discharge time of GCD curves and the capacitance vs current density plot (Fig. 5d). This drop-in specific capacitance at increased current density could be attributed to the

limited flow of electrolyte ions into the active material's inner site [67].

3.3.3. Electrochemical impedance spectroscopy

As illustrated in Fig. 6a, Nyquist plots were used to analyze the electrochemical impedance spectroscopy data and were displayed with an equivalent circuit inset. Three electrodes all displayed typical AC impedance characteristics of supercapacitors [68]. In the high-frequency region, the intersection of the curve at the real component reveals the bulk resistance of the electrochemical system. This includes ionic resistance from the electrolytes, intrinsic grain to grain resistance of the electrode, and contact resistance at the interphase between the active material and the substrate [69]. The radius of the semicircle in the high-frequency region displays the charge-transfer process, at the interface of the electrode and the electrolyte. As we approach lower frequencies the semicircle breaks into a 45° nearly vertical line which is related to the Warburg (W$_2$) diffusion of ions within the electrode interphase [70]. The EIS graphs demonstrated that RuSbO (7.62 Ω) had a greater Rs than RuSbO-G (6.5 Ω). The point where the semi-circle intersects with the real access is at a higher frequency. RuSbO and RuSbO-G have fitting R$_{ct}$ values of 4.30 Ω and 3.05 Ω respectively. The lower R$_{ct}$ in RuSbO-G will contribute to improved electrochemical properties. The slope of the 45° section of the curves in the intermediate frequency area was used to illustrate the Warburg resistance, which indicates ion diffusion/transport in the electrolyte and its relationship to frequencies.

Table 3

EIS curve fitting data of RuSbO and RuSbO-G electrode material.

Sample	R_s (Ω)	CPE (μF)	R_{ct} (Ω)	W^2 (Ω s- ½)	Phase angle (°)
RuSbO	7.627	66.2	4.3	29.34	56.8
RuSbO-G	6.471	580	3.05	13.51	60.7

The slanted vertical further confirms the pseudocapacitive contribution in the CV measurement. Furthermore, the Warburg resistance value is lower in the RuSbO-G (13.51 Ω) (Table 3). Because of the low charge transfer resistance and lower diffusion effect, very reversible processes

can occur at the interface, which is why both materials exhibit a rectangular voltammogram and maintain the rectangular feature even at high scan rates. The Bode plot from the EIS data is shown as the phase angle and total impedance plot in Fig. 6b & c respectively. The phase angle for RuSbO is 56.79° while that of RuSbO-G was 60.77°. The phase angle of RuSbO-G is closer to 90°, therefore, showing more capacitive behaviour. It is clear from the phase angle that the materials store charges utilizing both the EDL and the pseudocapacitive mechanisms. The magnitude of total impedance was similar in both materials with a magnitude of 0.8 Ω. The constant phase element (CPE) was also derived

Table 4

Compares RuSbO and RuSbO-G to other metal oxide-based electrode.

Materials	Electrolyte	Rate (mV s^{-1}) current (A g^{-1})	Capacitance (F g^{-1})	No. of cycles	Capacitance retained (%)	Ref.
AC/RuO$_2$	1 M Ni(NO$_3$)$_2$,	5[a]	248[b]	1000	93	[72]
Co$_3$O$_4$/RuO$_2$@NGO	3.0 KOH	0.5[c]	149[b]	5000	90	[73]
AC-Fe$_3$O$_4$	6 M KOH	0.5[d]	37.9[b]	500	82	[74]
RuO$_2$·xH$_2$O @ G	H$_3$PO$_4$/PVA	3.99[d]	210.14[f]	2000	94.40	[75]
BNWs-CFC	1 M Na2SO4	0.4[d]	24.48[e]	8000	57	[76]
BNWs-CFC	1 M H$_2$SO$_4$	0.2[d]	60.2[e]	8000	87	[76]
BNWs-CFC	4 M KOH	1[d]	44.9[e]	800	80	[76]
RuO$_2$@BCC	1 M H$_2$SO$_4$	10[d]	332[e]	5000	89.44	[77]
S-SnO$_2$NPs–RuO$_2$@BCC	1 M H$_2$SO$_4$	10[d]	649[e]	5000	92.78	[77]
CuSbS$_2$	1 M LiOH	0.25 mA	41.78[b]	2500	94.6	[21]
CuSbSexS$_2$ − x	LiOH	0.4 mA	48[b]	500	100	[78]
RuSbO	1 M Li$_2$SO$_4$	0.1[c]	95.33[b]	4800	82	Present work
RuSbO-G	1 M Li$_2$SO$_4$	0.1[c]	289.47[b]	4900	96	Present work

[a] mV s^{-1}.

[b] F g^{-1}.

[c] A g^{-1}.

[d] mA cm^{-2}.

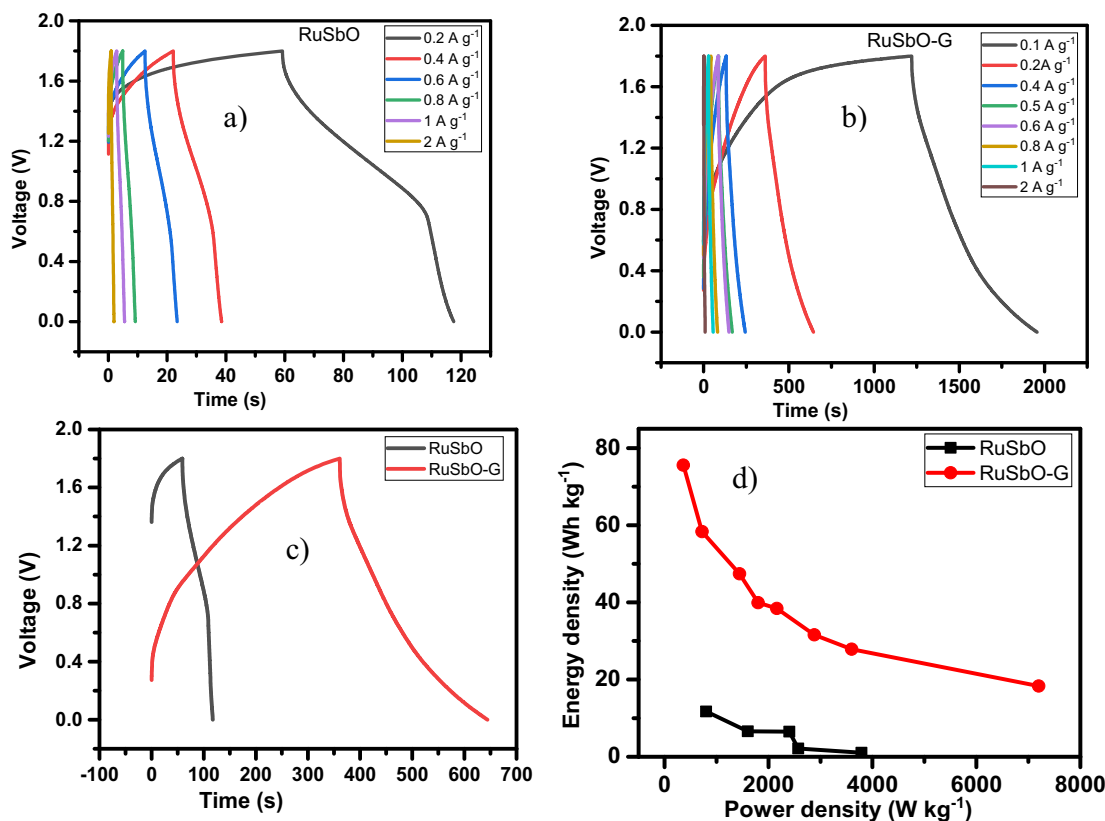[e] mF cm^{-2}.

[f] F cm^{-3}.

Fig. 7. AC//RuSbO and AC//RuSbO-G: a & b) GCD plots at different current densities, C) GCD plots comparing their charge and discharge profile at 0.2 A g^{-1} current density, d) is the Ragone plot. All analysis was done in 1 M Li$_2$SO$_4$ electrolyte.

from the Bode total impedance plot. The CPE impedance is given by

$$Z_{CPE} = a^{-1}(jw)^{-n} \qquad (4)$$

where a is the frequency-independent constant related to the roughness of the surface features, and the exponent n is determined by the slope of log Z vs. log f. The coefficient 'a' is resistive when $n = 0$, capacitive for $n = 1$ and a Warburg impedance (charge transfer impedance) for $n = 0.5$. The value of n for RuSbO and RuSbO-G was 0.37 and 0.3 respectively. The change in n confirms a change in the morphology of the material. The value demonstrates a slow transition from resistive to capacitive behaviour [71]. The total CPE values obtained from the fitted Nyquist plot are shown in Table 3. Table 4 compares RuSbO/RuSbO-G and previous metal oxide materials discussed in previous literature, using a 3-electrode system to determin their specific capacitances, current density, electrolyte, and other parameters. As per the table, our suggested material exhibited superior performance.

3.4. Device fabrication

In a two-electrode cell configuration with filter paper as the separator and 1 M Li_2SO_4 as the electrolyte, the active materials RuSbO and RuSbO-G (mass loading 14.9, 8.49 respectively) was coated on a Ni foam substrate and used in an asymmetric cell configuration, with activated carbon as the negative electrode. The CV of the RuSbO-G was done to determine the cell voltage, also the voltammogram of RuSbO-G and activated carbon was obtained, to determine the suitability of AC as the negative electrode (Supplementary document).

3.4.1. Galvanostatic charge-discharge

The capacitance of the RuSbO and RuSbO-G was calculated from the GCD profile (Fig. 7a, b). The GCD profile is near triangular confirming the electric double layer capacitive charge storage mechanism [66]. It also shows that the redox activity is a pseudocapacitive electrochemical absorption-desorption process, happening at the surface of the RuSbO and RuSbO-G electrode [79]. The timing for the charge and discharge process is near similar, indicating a high Coulombic efficiency and electrochemical reversibility [65]. These observations are consistent with the oxidation and reduction profiles reported in the CV curves. The specific capacitance was determined using the equation

$$C_s = \frac{I \times t}{m \times V - IR_{drop}} \qquad (5)$$

where I is the constant current, m is the active material mass, and t is the discharge time corresponding to the voltage change V [22]. The RuSbO-G electrode has the highest specific capacitance at the same current density when compared to RuSbO electrodes. The capacitance of the RuSbO-G electrode, for example, reached up to 129.71 F g^{-1} at 0.2 A g^{-1}, while RuSbO was 26.09 F g^{-1} at 0.2 A g^{-1}. This is due to graphene's porous microstructure, which facilitates electrolyte infiltration and contributes to the development of electric double-layer capacitance. A small IR drop was observed at the beginning of the discharge curve, especially for RuSbO in 1 MLi_2SO_4 implying the low internal resistance within the electrode. It was observed that the specific capacitance decreased with an increase in the current load. At the highest current density of 2 A g^{-1} the specific capacitance of the RuSbO-G reached 40.71 F g^{-1} retaining 31 % of its capacitance, while that of RuSbO was at 2.27 F g^{-1}, retaining only about 8 % of its capacitance. Optimizing this materials surface area by using other synthesis routes that will reduce agglomeration might be a good way of improving the rate capability of this material. The two most important metrics for determining the performance of an energy storage device are energy density and power density. The following equations were used to compute specific energy and power:

Table 5
Capacitance, ED and PD of activated carbon//RuSbO carbon device from the GCD data.

RuSbO			
Current density (A g^{-1})	Capacitance (F g^{-1})	Power density (W kg^{-1})	Energy density (W h kg^{-1})
0.2	26.09	800.00	11.74
0.4	14.67	1600.00	6.60
0.6	14.45	2400.00	6.50
0.8	8.36	3200.00	3.76
1	4.71	2571.43	2.12
2	2.27	3789.47	1.02

Table 6
Capacitance, ED and PD of activated carbon//RuSbO-G carbon device from the GCD data.

RuSbO-G			
Current density (A g^{-1})	Capacitance (F g^{-1})	Power density (W kg^{-1})	Energy density (W h kg^{-1})
0.1	167.96	360.00	75.58
0.2	129.71	720.00	58.37
0.4	105.39	1440.00	47.42
0.5	88.67	1800.00	39.90
0.6	85.33	2160.00	38.40
0.8	70.17	2880.00	31.58
1	61.93	3600.00	27.87
2	40.71	7200.00	18.32

$$E_{sp}\left(\frac{Wh}{Kg}\right) = \frac{CV^2}{2m} \times \frac{1}{3.6} \qquad (6)$$

$$P_{max}\left(\frac{W}{Kg}\right) = \frac{E}{\triangle t} \times 3600 \qquad (7)$$

where C (F g^{-1}) is the specific capacitance determined from Eq. (4), V is the maximum working potential, m (kg) is the mass of the active material in the electrode, and $\triangle t$ is the capacitors discharge time. Fig. 7d is the Ragone plot showing the relationship between the asymmetric device's energy density and power density at various current densities. An ideal supercapacitor device would have a high energy density while also having a high-power density. The asymmetric Cs cell delivered a maximum energy density of 75.58 W h kg^{-1}, at a power density of 360 W kg^{-1}, at 0.1 A g^{-1} current load for RuSbO-G. At 0.2 A g^{-1} the capacitance of the composite decreased to 58.32 W h kg^{-1}, at a power density of 720 W kg^{-1}, while at the same current density, RuSbO delivered an energy density of 11.74 W h kg^{-1}, at a power density of 800 W kg^{-1}. At a high power of 7200 W kg^{-1}, the RuSbO-G composite maintained an energy density of 18.2 W h kg^{-1}. The energy density and power density were enhanced by the addition of graphene [80]. Details of the GCD result are recorded in Tables 5 and 6.

3.4.2. Electrochemical impedance spectroscopy

Fig. 8a is the Nyquist plot of the RuSbO and RuSbO-G asymmetric device. The inset is the fitted equivalent circuit data, and the parameters obtained are represented in Table 7 below. It can be seen that the EIS which is primarily affected by the electrolyte is higher in the RuSbO-G (2.13 Ω) than in the RuSbO (1.3 Ω) material [81]. However, the charge-transfer resistance at the interface of the electrode and the electrolyte was very much lower for RuSbO-G (2.82 Ω) as compared to RuSbO (19.67 Ω), as can be seen in the semi-circle at the high-frequency region of the Nyquist plot. This shows that more facile charge transfer occurred between the Li^+/SO_4^{-2} ions and the RuSbO-G [81,82]. The presence of a defined and short Warburg area section in the RuSbO-G device when compared to the RuSbO device reveals that the ions in the electrolyte have a short and equal diffusion path length. As a result of
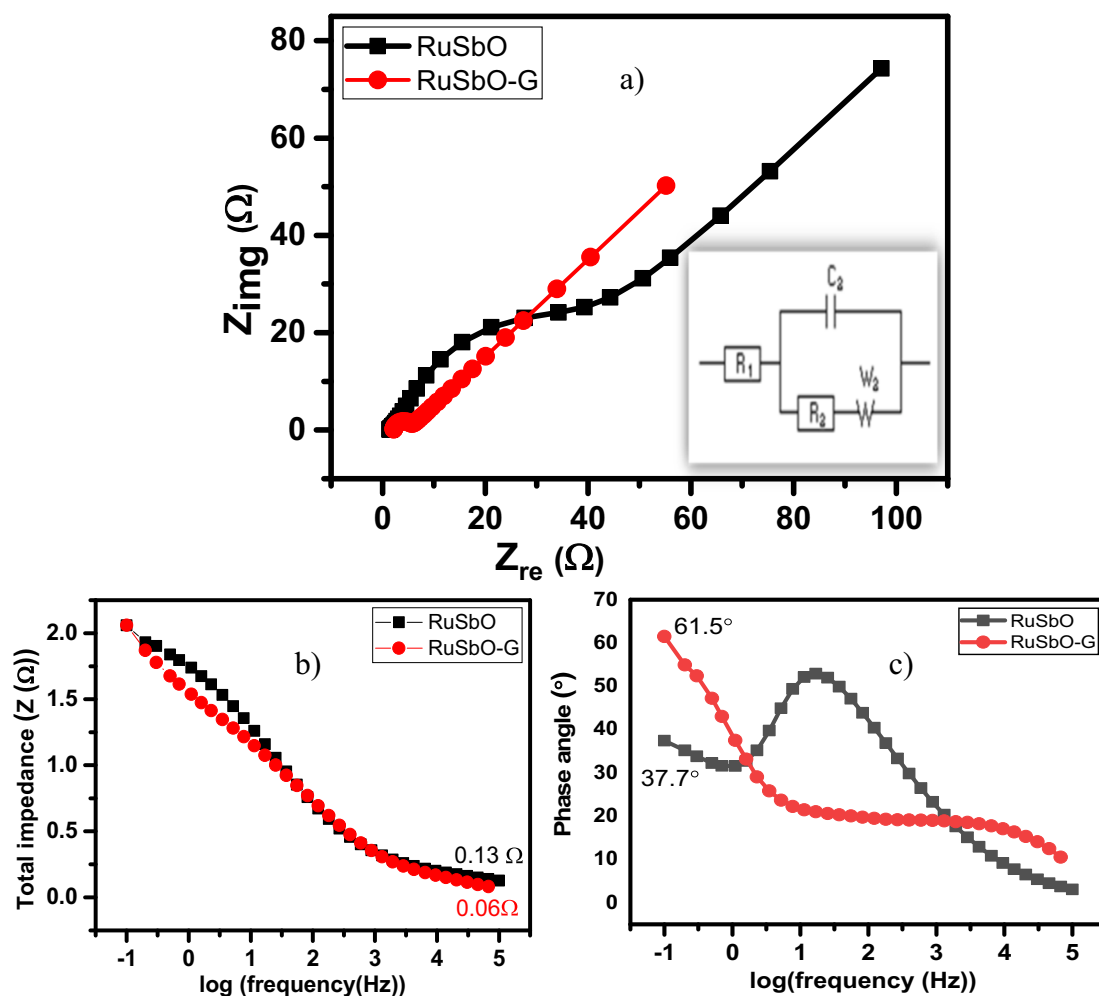
Fig. 8. EIS results represented as a) Nyquist plot (the inset is the equivalent circuit), b) bode plots, c) total impedance plots.

Table 7
EIS curve fitting data of AC//RuSbO and AC//RuSbO-G electrode material.

Electrolytes	R_s (Ω)	CPE (μF)	R_{ct} (Ω)	W^2 (Ω s- ½)	Phase angle (°)
RuSbO	1.3	149	19.67	55.99	61.5
RuSbO-G	2.13	28	2.82	39.83	37.7

the low charge transfer resistance and decreased diffusion activity, relatively reversible processes can occur at the interface [83]. The Bode plot from the EIS data is shown as the phase angle and total impedance plot in Fig. 8b & c. The phase angle of RuSbO is 37.7° while that of the RuSbO-G device is at 61.05°. The composite indicates a more capacitive behaviour than the RuSbO device as its value is closer to 90° which is the ideal phase angle for an EDLC. This further confirms the contribution of both EDLC and pseudocapacitance charge storage mechanisms in the composite material. The RuSbO material shows a greater resistance in transiting from resistive to capacitive behaviour, hence its low phase angle. The magnitude of total impedance had a value of 0.13 Ω for RuSbO and 0.06 Ω for RuSbO-G, confirming the lower resistance in the RuSbO-G as seen in the Nyquist plot and the phase angle plot.

3.4.3. Cycle life

The cycling performance of both ASC is evaluated through ~4800 C*V* cycles at a current density of 0.5 A g^{-1} (Fig. 9a). The ASC of RuSbO retains about 82 % of its first cycle capacitance during the test, within a voltage window of 0 to 1.8 V. A comparison of Nyquist plots before and

after the cycle test (Fig. 9a inset (i)) demonstrates an increase in the semi-circle area, therefore the charge transfer resistance increased during circling (Table 8). A similar variation of the CV plot before and after circling (Fig. 9a inset (ii)) implies a variation in the morphology of the material after cycling. The ASC of RuSbO-G on the other hand showed a better cycling performance, preserving about 96 % of its first cycle capacitance during the test. Thus, demonstrating a better electrode performance and electrolyte stability within the same voltage window (Fig. 9b). The curve shows an initial loss in capacitance from 0 to about 280 cycles, then an increase in capacitance until about 1800 cycles, and finally a steady capacitance for the remaining 4900 cycles. The initial rise in capacitance could be attributed to electrode material activation caused by enhanced wetting of the electrode, making it easier for hydrated ions to diffuse during cycling [84]. A comparison of Nyquist plots before and after the cycle test (Fig. 9b inset (i)) demonstrates a minor change in the device's Ohmic resistance during cycling, confirming the outstanding stability of electrode materials (Table 8). No significant change in the shape of the voltammogram was observed (Fig. 9b inset (ii)). However, the area under the CV curve decreased a little, showing that the RuSbO-G device is more stable than the RuSbO device. Therefore, the addition of graphene to the RuSbO increased the stability of the material [85].

4. Conclusion

For the first time, RuSbO and RuSbO-G were synthesized and used as an electrode material for a supercapacitor device. The pristine material
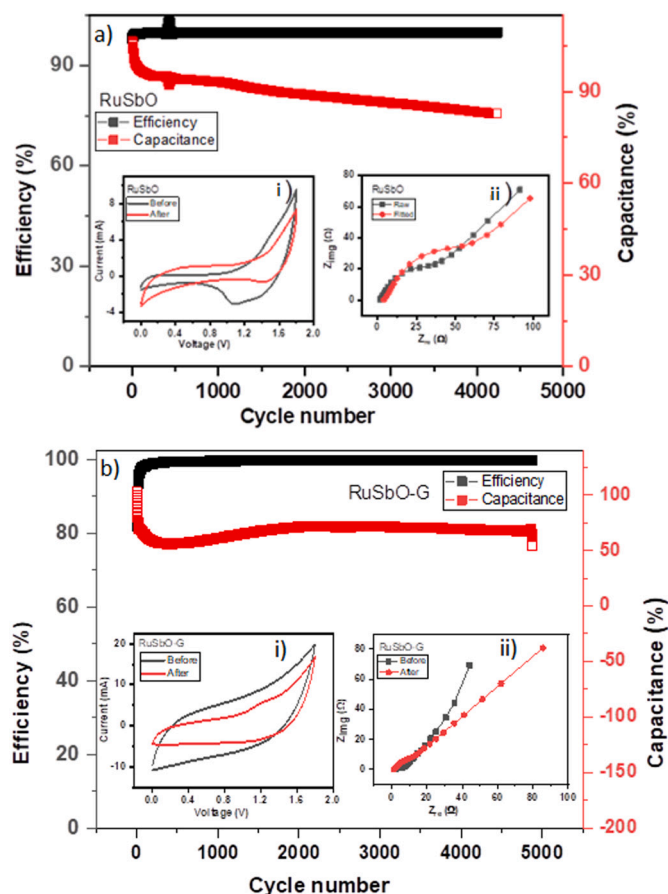
Fig. 9. Cycling stability of a) AC//RuSbO and b) AC//RuSbO-G supercapacitor over 4500 cycles in 1 M Li$_2$SO$_4$. The inset in a & b) is the CV plot (50 mV s^{-1}) and EIS plot before and after cycling.

Table 8
EIS curve fitting data of AC//RuSbO and AC//RuSbO-G electrode material after cycling.

	RuSbO		RuSbO-G	
	R_s (Ω)	R_{ct} (Ω)	R_s (Ω)	R_{ct} (Ω)
Before	1.33	19.67	2.13	2.6
After	3.81	30.83	1.16	3.65

RuSbO and the composite RuSbO-G were prepared via microwave-assisted methods and were morphologically and structurally characterized to ascertain the successful synthesis of the material. The average particle size of the pristine RuSbO was 37.30 nm from the XRD data, while those of RuSbO-G were 36.33 nm with an increased interlayer spacing of 0.8 nm showing successful attachment of the graphene material to the composite. Further electrochemical characterization revealed the capacitive nature of the novel material and its charge storage mechanism. In all the experiments, RuSbO-G showed better electrochemical performance than the pristine material. This is because, graphene must have acted as a dispersing agent for the RuSbO species and prevented the nanoparticles from agglomerating thus, providing better ionic pathways for the electrolyte ions. While the RuSbO nanoparticles must have acted as spacers for the graphene sheet to prevent severe agglomeration, thus harnessing the unique 2D characteristics of graphene. RuSbO-G electrode was used to fabricate an asymmetric capacitor, with a capacitance of 167.96 F g^{-1} at a current density of 0.1 A g^{-1}. The composite material showed impressive cyclic stability and maintained high Columbic efficiency throughout its cycle life, owing to

the mechanical stability provided by the graphene network. These studies open a new dimension for the exploration of new categories of nanomaterials particularly the antimonide based nanomaterials for supercapacitor application.

CRediT authorship contribution statement

All persons who meet authorship criteria are listed as authors, and all authors certify that they have participated sufficiently in the work to take public responsibility for the content, including participation in the concept, design, analysis, writing, or revision of the manuscript.

Declaration of competing interest

The authors declare that they have no known competing financial interests or personal relationships that could have appeared to influence the work reported in this paper.

Data availability

Data will be made available on request.

Acknowledgement

Appendix A. Supplementary data

Supplementary data to this article can be found online at https://doi.org/10.1016/j.est.2023.106853.

References

[1] P.D. Wall, Scientists and the CIA, Science(80-.) 136 (1962) 173, https://doi.org/10.1126/science.136.3511.173.
[2] C. Clark, World population, Nature 181 (1958) 1235–1236, https://doi.org/10.1038/1811235a0.
[3] I. Yang, D. Kwon, M.S. Kim, J.C. Jung, A comparative study of activated carbon aerogel and commercial activated carbons as electrode materials for organic electric double-layer capacitors, Carbon N. Y. 132 (2018) 503–511, https://doi.org/10.1016/j.carbon.2018.02.076.
[4] S. Han, F. Hou, X. Yuan, J. Liu, X. Yan, S. Chen, Continuous hierarchical carbon nanotube/reduced graphene oxide hybrid films for supercapacitors, Electrochim. Acta 225 (2017) 566–573, https://doi.org/10.1016/j.electacta.2016.12.159.
[5] G. Wang, L. Zhang, J. Zhang, A review of electrode materials for electrochemical supercapacitors, Chem. Soc. Rev. 41 (2012) 797–828, https://doi.org/10.1039/c1cs15060j.
[6] S. Chen, R. Ramachandran, V. Mani, R. Saraswathi, Recent advancements in electrode materials for the high- performance, in: Electrochemical Supercapacitors: A Review 9, 2014, pp. 4072–4085.
[7] D. Galizzioli, F. Tantardini, S. Trasatti, Ruthenium dioxide: a new electrode material. I. Behaviour in acid solutions of inert electrolytes, J. Appl. Electrochem. 4 (1974) 57–67, https://doi.org/10.1007/BF00615906.
[8] M. Ates, C. Fernandez, Ruthenium oxide–carbon-based nanofiller-reinforced conducting polymer nanocomposites and their supercapacitor applications, Polym. Bull. (2018) 1–19, https://doi.org/10.1007/s00289-018-2492-x.
[9] Y. Guo, W. Zhang, Y. Sun, M. Dai, Ruthenium nanoparticles stabilized by mercaptan and acetylene derivatives with supercapacitor application, MethodsX 5 (2018) 795–796, https://doi.org/10.1016/j.mex.2018.07.004.
[10] J.H. Jang, A. Kato, K. Machida, K. Naoi, Supercapacitor performance of hydrous ruthenium oxide electrodes prepared by electrophoretic deposition, J. Electrochem. Soc. 153 (2006) A321, https://doi.org/10.1149/1.2138672.
[11] H. Li, R. Wang, R. Cao, Physical and electrochemical characterization of hydrous ruthenium oxide/ordered mesoporous carbon composites as supercapacitor, Microporous Mesoporous Mater. 111 (2008) 32–38, https://doi.org/10.1016/j.micromeso.2007.07.002.
[12] K.Y. Kumar, S. Archana, R. Namitha, B.P. Prasanna, S.C. Sharma, M.S. Raghu, Ruthenium oxide nanostring clusters anchored graphene oxide nanocomposites for high-performance supercapacitors application, Mater. Res. Bull. 107 (2018) 347–354, https://doi.org/10.1016/j.materresbull.2018.08.011.

[13] D. Rosestolato, G. Battaglin, S. Ferro, Charge-storage process of stoichiometric and nanostructured ruthenium nitride thin films, Batteries 1 (2015) 11–21, https://doi.org/10.3390/batteries1010011.

[14] P. Suktha, N. Phattharasupakun, M. Sawangphruk, Transparent supercapacitors of 2 nm ruthenium oxide nanoparticles decorated on a 3D nitrogen-doped graphene aerogel, sustain, Energy Fuel 2 (2018) 1799–1805, https://doi.org/10.1039/C8SE00177D.

[15] D. Rosestolato, G. Battaglin, S. Ferro, Electrochemical properties of stoichiometric RuN film prepared by rf-magnetron sputtering: a preliminary study, Electrochem. Commun. 49 (2014) 9–13, https://doi.org/10.1016/j.elecom.2014.09.019.

[16] S. Bouhtiyya, R. Lucio Porto, B. Laïk, P. Boulet, F. Capon, J.P. Pereira-Ramos, T. Brousse, J.F. Pierson, Application of sputtered ruthenium nitride thin films as electrode material for energy-storage devices, Scr. Mater. 68 (2013) 659–662, https://doi.org/10.1016/j.scriptamat.2013.01.030.

[17] R. Bolagam, S. Um, L-cysteine-assisted synthesis of ruthenium sulfide/thermally reduced graphene oxide nanocomposites: promising electrode materials for high-performance energy storage applications, Electrochim. Acta 281 (2018) 571–581, https://doi.org/10.1016/j.electacta.2018.06.004.

[18] F.J. Berry, C.D. Gibbs, C. Greaves, Structural properties of the molybdenum-ruthenium telluride of composition Mo4.5Ru1.5Te8, J. Solid State Chem. 92 (1991) 148–153, https://doi.org/10.1016/0022-4596(91)90251-C.

[19] T. Cao, Y. Shi, Y. Jiang, N. Cai, Q. Gong, Performance enhancement of liquid antimony anode fuel cell by in-situ electrochemical assisted oxidation process, Energy 125 (2017) 526–532, https://doi.org/10.1016/j.energy.2017.02.106.

[20] E. Martínez-Periñán, M.P. Down, C. Gibaja, E. Lorenzo, F. Zamora, C.E. Banks, Antimonene: a novel 2D nanomaterial for supercapacitor applications, Adv. Energy Mater. 8 (2018) 1–8, https://doi.org/10.1002/aenm.201702606.

[21] V.K. Mariappan, K. Krishnamoorthy, P. Pazhamalai, S. Sahoo, S.J. Kim, Layered famatinite nanoplates as an advanced pseudocapacitive electrode material for supercapacitor applications, Electrochim. Acta 275 (2018) 110–118, https://doi.org/10.1016/j.electacta.2018.04.126.

[22] J. Sun, H.W. Lee, M. Pasta, H. Yuan, G. Zheng, Y. Sun, Y. Li, Y. Cui, A phosphorene-graphene hybrid material as a high-capacity anode for sodium-ion batteries, Nat. Nanotechnol. 10 (2015) 980–985, https://doi.org/10.1038/nnano.2015.194.

[23] N.A. Luechinger, N. Booth, G. Heness, S. Bandyopadhyay, R.N. Grass, W.J. Stark, Surfactant-free, melt-processable metal-polymer hybrid materials: use of graphene as a dispersing agent, Adv. Mater. 20 (2008) 3044–3049, https://doi.org/10.1002/adma.200800026.

[24] S. Korkmaz, F. Meydaneri Tezel, A. Kariper, A. Serin, Effects of deposition temperatures on the supercapacitor cathode performances of GO:SnSbS/Si thin films, J. Energy Storage 33 (2021), 102116, https://doi.org/10.1016/j.est.2020.102116.

[25] Z. Lin, L. Xu, Y. Ling, X. Zhou, L. Ma, Solvothermal synthesis of antimony phosphate hierarchical microspindles and their capacitive property, Mater. Lett. 227 (2018) 264–267, https://doi.org/10.1016/j.matlet.2018.05.104.

[26] X. Wang, J. Wang, H. Cheng, P. Yu, J. Ye, L. Mao, Graphene as a spacer to layer-by-layer assemble electrochemically functionalized nanostructures for molecular bioelectronic devices, Langmuir 27 (2011) 11180–11186, https://doi.org/10.1021/la202018r.

[27] I.S. El-Hallag, M.N. El-Nahass, S.M. Youssry, R. Kumar, M.M. Abdel-Galeil, A. Matsuda, Facile in-situ simultaneous electrochemical reduction and deposition of reduced graphene oxide embedded palladium nanoparticles as high performance electrode materials for supercapacitor with excellent rate capability, Electrochim. Acta 314 (2019) 124–134, https://doi.org/10.1016/j.electacta.2019.05.065.

[28] W. Sobieski, S. Lipiński, The influence of particle size distribution on parameters characterizing the spatial structure of porous beds, Granul. Matter 21 (2019) 1–15, https://doi.org/10.1007/s10035-019-0866-x.

[29] N. Ouchlyama, T. Tanaka, Porosity estimation from particle size distribution, Ind. Eng. Chem. Fundam. 25 (1986) 125–129, https://doi.org/10.1021/i100021a019.

[30] E. Antolini, F. Cardellini, Formation of carbon supported PtRu alloys: an XRD analysis, J. Alloys Compd. 315 (2001) 118–122, https://doi.org/10.1016/S0925-8388(00)01260-3.

[31] A.S. Patil, J.L. Gunjakar, C.D. Lokhande, U.M. Patil, S.V. Sadavar, N.S. Padalkar, R. B. Shinde, M.M. Wagh, J.S. Bagi, Nanocrystalline copper-chromium-layered double hydroxide with tunable interlayer anions for electrochemical capacitor application, Synth. Met. 264 (2020), 116371, https://doi.org/10.1016/J.SYNTHMET.2020.116371.

[32] R.S. Rajaura, S. Srivastava, V. Sharma, P.K. Sharma, C. Lal, M. Singh, H.S. Palsania, Y.K. Vijay, Role of interlayer spacing and functional group on the hydrogen storage properties of graphene oxide and reduced graphene oxide, Int. J. Hydrog. Energy 41 (2016) 9454–9461, https://doi.org/10.1016/J.IJHYDENE.2016.04.115.

[33] P.R. Deshmukh, S.N. Pusawale, A.D. Jagadale, C.D. Lokhande, Supercapacitive performance of hydrous ruthenium oxide (RuO·nH2O) thin films deposited by SILAR method, J. Mater. Sci. 473 (47) (2011) 1546–1553, https://doi.org/10.1007/S10853-011-5946-1.

[34] W. Xu, H. Wang, R. Liu, X. Zhao, J. Qu, The mechanism of antimony(III) removal and its reactions on the surfaces of Fe–Mn binary oxide, J. Colloid Interface Sci. 363 (2011) 320–326, https://doi.org/10.1016/J.JCIS.2011.07.026.

[35] P.H.S. Borges, A.C. Catto, E. Longo, E. Nossol, Electrochemical synthesis of reduced graphene oxide/ruthenium oxide hexacyanoferrate nanocomposite film and its application for ranitidine detection, J. Electroanal. Chem. 878 (2020), 114558, https://doi.org/10.1016/J.JELECHEM.2020.114558.

[36] J. Bin Wu, M.L. Lin, X. Cong, H.N. Liu, P.H. Tan, Raman spectroscopy of graphene-based materials and its applications in related fields, Chem. Soc. Rev. 47 (2018) 1822–1873, https://doi.org/10.1039/c6cs00915h.

[37] M. Assebban, C. Gibaja, M. Fickert, I. Torres, E. Weinreich, S. Wolff, R. Gillen, J. Maultzsch, M. Varela, S.Tan Jun Rong, K.P. Loh, E.G. Michel, F. Zamora, G. Abellán, Unveiling the oxidation behavior of liquid-phase exfoliated antimony nanosheets, 2D Mater. 7 (2020), https://doi.org/10.1088/2053-1583/ab755e.

[38] N.E. Drewett, I.M. Aldous, J. Zou, L.J. Hardwick, In situ raman spectroscopic analysis of the lithiation and sodiation of antimony microparticles, Electrochim. Acta 247 (2017) 296–305, https://doi.org/10.1016/j.electacta.2017.07.030.

[39] T.K. Das, S. Banerjee, M. Pandey, B. Vishwanadh, R.J. Kshirsagar, V. Sudarsan, Effect of surface functional groups on hydrogen adsorption properties of pd dispersed reduced graphene oxide, Int. J. Hydrog. Energy 42 (2017) 8032–8041, https://doi.org/10.1016/j.ijhydene.2016.12.024.

[40] F.T. Johra, J.W. Lee, W.G. Jung, Facile and safe graphene preparation on solution based platform, J. Ind. Eng. Chem. 20 (2014) 2883–2887, https://doi.org/10.1016/j.jiec.2013.11.022.

[41] X. Zhang, X. Chen, C. Chen, T. Liu, M. Liu, C. Zhang, T. Huang, A. Yu, Ruthenium oxide modified hierarchically porous boron-doped graphene aerogels as oxygen electrodes for lithium-oxygen batteries, RSC Adv. 8 (2018) 39829–39836, https://doi.org/10.1039/C8RA08763F.

[42] H.K. Hassan, N.F. Atta, M.M. Hamed, A. Galal, T. Jacob, Ruthenium nanoparticles-modified reduced graphene prepared by a green method for high-performance supercapacitor application in neutral electrolyte, RSC Adv. 7 (2017) 11286–11296, https://doi.org/10.1039/c6ra27415c.

[43] S. Wolff, S. Roscher, F. Timmermann, M.V. Daniel, F. Speck, M. Wanke, M. Albrecht, T. Seyller, Quasi-freestanding graphene on SiC(0001) by Ar-mediated intercalation of antimony: a route toward intercalation of high-vapor-pressure elements, Ann. Phys. 531 (2019), https://doi.org/10.1002/andp.201900199.

[44] R. Vinoth, S.G. Babu, V. Bharti, V. Gupta, M. Navaneethan, S.V. Bhat, C. Muthamizhchelvan, P.C. Ramamurthy, C. Sharma, D.K. Aswal, Y. Hayakawa, B. Neppolian, Ruthenium based metallopolymer grafted reduced graphene oxide as a new hybrid solar light harvester in polymer solar cells, Sci. Rep. 7 (2017) 1–14, https://doi.org/10.1038/srep43133.

[45] R. Mondal, K. Sarkar, S. Dey, D. Majumdar, S.K. Bhattacharya, P. Sen, S. Kumar, Magnetic, pseudocapacitive, and H2O2-electrosensing properties of self-assembled superparamagnetic Co0.3Zn0.7Fe2O4 with enhanced saturation magnetization, ACSOmega 4 (2019) 12632–12646, https://doi.org/10.1021/acsomega.9b01362.

[46] G. Chen, S. Wu, L. Hui, Y. Zhao, J. Ye, Z. Tan, W. Zeng, Z. Tao, L. Yang, Y. Zhu, Assembling carbon quantum dots to a layered carbon for high-density supercapacitor electrodes, Sci. Rep. 6 (2016) 1–9, https://doi.org/10.1038/srep19028.

[47] A.M. Teli, S.A. Beknalkar, S.A. Pawar, D.P. Dubal, Effect of concentration on the charge storage kinetics, Energies 13 (2020) 6124.

[48] Y. Guo, W. Zhang, Y. Sun, M. Dai, Ruthenium nanoparticles stabilized by mercaptan and acetylene derivatives with supercapacitor application, Electrochim. Acta 270 (2018) 284–293, https://doi.org/10.1016/j.electacta.2018.03.037.

[49] H. Xue, K. Chen, Q. Zhou, D. Pan, Y. Zhang, Y. Shen, Antimony selenide/graphene oxide composite for sensitive photoelectrochemical detection of DNA methyltransferase activity, J. Mater. Chem. B 7 (2019) 6789–6795, https://doi.org/10.1039/c9tb01541h.

[50] Y. Guo, Z. Li, Y. Xia, Y. Wei, J. Zhang, Y. Wang, H. He, Facile synthesis of ruhtenium nanoparticles capped by graphene and thiols for high-performance supercapacitors, Electrochim. Acta 391 (2021), 138990, https://doi.org/10.1016/j.electacta.2021.138990.

[51] Y. Guo, Y. Wu, R. Cao, S. Zheng, Y. Yang, M. Chen, Platinum nanoparticles functionalized with acetylene derivatives and the influence of ligand length on their electrocatalytic activity, J. Electroanal. Chem. 785 (2017) 159–165, https://doi.org/10.1016/j.jelechem.2016.12.035.

[52] Z. Sun, H. Chang, Graphene and graphene-like two-dimensional materials in photodetection: mechanisms and methodology, ACS Nano 8 (2014) 4133–4156, https://doi.org/10.1021/NN500508C.

[53] S. Akshatha, S. Sreenivasa, K.Y. Kumar, S. Archana, M.K. Prashanth, B.P. Prasanna, P. Chakraborty, P. Krishnaiah, M.S. Raghu, H. Alrobei, Rutile, mesoporous ruthenium oxide decorated graphene oxide as an efficient visible light driven photocatalyst for hydrogen evolution reaction and organic pollutant degradation, Mater. Sci. Semicond. Process. 116 (2020), 105156, https://doi.org/10.1016/j.mssp.2020.105156.

[54] F. El-Tantawy, A.A. Al-Ghamdi, A.A. Al-Ghamdi, Y.A. Al-Turki, A. Alshahrie, F. Al-Hazmi, O.A. Al-Hartomy, Optical properties of nanostructured ruthenium dioxide thin films via sol–gel approach, J. Mater. Sci. Mater. Electron. 28 (2017) 52–59, https://doi.org/10.1007/s10854-016-5491-4.

[55] P. Molaei, I. Kazeminezhad, Extended photocurrent performance of antimony trisulfide/reduced graphene oxide composite prepared via a facile hot-injection route, Ceram. Int. 44 (2018) 13191–13196, https://doi.org/10.1016/j.ceramint.2018.04.144.

[56] Z. Li, Y. Mi, X. Liu, S. Liu, S. Yang, J. Wang, Flexible graphene/MnO2 composite papers for supercapacitor electrodes, J. Mater. Chem. 21 (2011) 14706–14711, https://doi.org/10.1039/c1jm11941a.

[57] H.L. Girard, H. Wang, A.L. D'Entremont, L. Pilon, Enhancing faradaic charge storage contribution in hybrid pseudocapacitors, Electrochim. Acta 182 (2015) 639–651, https://doi.org/10.1016/j.electacta.2015.09.070.

[58] B.J. Choudhury, K. Roy, V.S. Moholkar, Improvement of supercapacitor performance through enhanced interfacial interactions induced by sonication, Ind. Eng. Chem. Res. 60 (2021) 7611–7623, https://doi.org/10.1021/acs.iecr.1c00279.

[59] J. Shen, J. Wu, L. Pei, M.T.F. Rodrigues, Z.Q. Zhang, F. Zhang, X. Zhang, P. M. Ajayan, M. Ye, CoNi2S4-graphene-2D-MoSe2 as an advanced electrode material for supercapacitors, Adv. Energy Mater. 6 (2016) 1–8, https://doi.org/10.1002/aenm.201600341.

[60] V. Venezlan, in: "Inner" and "Outer" Active Surface Electrodes of RuO, 1989, pp. 5–9.

[61] T. Wang, H.C. Chen, F. Yu, X.S. Zhao, H. Wang, Boosting the cycling stability of transition metal compounds-based supercapacitors, Energy Storage Mater. 16 (2019) 545–573, https://doi.org/10.1016/j.ensm.2018.09.007.

[62] M. Guo, L. Ye, L. Zhao, Solid-state-grinding method to synthesize NiCoFe alloy/ NiCoFe–OH nanosheets for asymmetric supercapacitor, J. Alloys Compd. 850 (2021), 156787, https://doi.org/10.1016/j.jallcom.2020.156787.

[63] E.E. Mathew, M. Balachandran, Crumpled and porous graphene for supercapacitor applications: a short review, Carbon Lett. 31 (2021) 537–555, https://doi.org/10.1007/s42823-021-00229-2.

[64] J. Yan, T. Wei, W. Qiao, B. Shao, Q. Zhao, L. Zhang, Z. Fan, Rapid microwave-assisted synthesis of graphene nanosheet/Co 3O4 composite for supercapacitors, Electrochim. Acta 55 (2010) 6973–6978, https://doi.org/10.1016/j.electacta.2010.06.081.

[65] T. Pettong, P. Iamprasertkun, A. Krittayavathananon, P. Sukha, P. Sirisinudomkit, A. Seubsai, M. Chareonpanich, P. Kongkachuichay, J. Limtrakul, M. Sawangphruk, High-performance asymmetric supercapacitors of MnCo2O4 nanofibers and N-doped reduced graphene oxide aerogel, ACS Appl. Mater. Interfaces 8 (2016) 34045–34053, https://doi.org/10.1021/acsami.6b09440.

[66] C. Wang, J. Zhao, S. Luo, X. Yu, Improved pseudocapacitive performance of graphene architectures modulating by Nitrogen/Phosphorus dual-doping and steam-activation, Macromol. Res. 29 (2021) 582–588, https://doi.org/10.1007/s13233-021-9075-7.

[67] M. Dvoyashkin, D. Leistenschneider, J.D. Evans, M. Sander, L. Borchardt, Revealing the impact of hierarchical pore organization in supercapacitor electrodes by coupling ionic dynamics at micro- and macroscales, Adv. Energy Mater. 11 (2021) 2100700, https://doi.org/10.1002/aenm.202100700.

[68] D. Qu, Studies of the activated mesocarbon microbeads used in double-layer supercapacitors, J. Power Sources 109 (2002) 403–411.

[69] D. Mandal, P. Routh, A.K. Mahato, A.K. Nandi, Electrochemically modified graphite paper as an advanced electrode substrate for supercapacitor application, J. Mater. Chem. A 7 (2019) 17547–17560, https://doi.org/10.1039/c9ta04496e.

[70] Y. Gong, D. Li, Q. Fu, C. Pan, Influence of graphene microstructures on electrochemical performance for supercapacitors, Prog. Nat. Sci. Mater. Int. 25 (2015) 379–385, https://doi.org/10.1016/j.pnsc.2015.10.004.

[71] H. Wei, C. He, J. Liu, H. Gu, Y. Wang, X. Yan, J. Guo, D. Ding, N.Z. Shen, X. Wang, S. Wei, Z. Guo, Electropolymerized polypyrrole nanocomposites with cobalt oxide coated on carbon paper for electrochemical energy storage, Polymer (Guildf) 67 (2015) 192–199, https://doi.org/10.1016/J.POLYMER.2015.04.064.

[72] R.K. Guduru, J.C. Icaza, S.K. Pudi, Electrochemical characterization of RuO2 and activated carbon (AC) electrodes using multivalent Ni(NO3)2 electrolyte for charge storage applications, J. Energy Storage 34 (2021) 102170, https://doi.org/10.1016/j.est.2020.102170.

[73] S. Ramesh, H. Kim, H. Soo, K.J. Kim, in: Effect of Ruthenium Oxide on the Capacitance and Gas-sensing Performances of Cobalt Oxide@nitrogen-doped Graphene Oxide Composites, 2021, pp. 1–13, https://doi.org/10.1002/er.7049.

[74] D. Xuan, W. Chengyang, C. Mingming, J. Yang, W. Jin, Electrochemical performances of nanoparticle Fe3O 4/activated carbon supercapacitor using KOH electrolyte solution, J. Phys. Chem. C 113 (2009) 2643–2646, https://doi.org/10.1021/jp8088269.

[75] X. Li, D. Liu, X. Yin, C. Zhang, P. Cheng, H. Guo, W. Song, J. Wang, Hydrated ruthenium dioxides @ graphene based fiber supercapacitor for wearable electronics, J. Power Sources 440 (2019), 227143, https://doi.org/10.1016/j.jpowsour.2019.227143.

[76] Q. Xue, H. Gan, Y. Huang, M. Zhu, Z. Pei, H. Li, S. Deng, F. Liu, C. Zhi, Boron element nanowires electrode for supercapacitors, Adv. Energy Mater. 8 (2018) 1–8, https://doi.org/10.1002/aenm.201703117.

[77] C. Mevada, M. Mukhopadhyay, High mass loading tin oxide-ruthenium oxide-based nanocomposite electrode for supercapacitor application, J. Energy Storage 31 (2020), 101587, https://doi.org/10.1016/j.est.2020.101587.

[78] K. Ramasamy, R.K. Gupta, S. Palchoudhury, S. Ivanov, A. Gupta, Layer-structured copper antimony chalcogenides (CuSbSexS2-x): stable electrode materials for supercapacitors, Chem. Mater. 27 (2015) 379–386, https://doi.org/10.1021/cm5041166.

[79] A. Noori, M.F. El-kady, M.S. Rahmanifar, R.B. Kaner, M.F. Mousavi, Chem soc rev metrics for batteries, supercapacitors and beyond, Chem. Soc. Rev. (2019), https://doi.org/10.1039/c8cs00581h.

[80] A.G. Pandolfo, A.F. Hollenkamp, Carbon properties and their role in supercapacitors, J. Power Sources 157 (2006) 11–27, https://doi.org/10.1016/j.jpowsour.2006.02.065.

[81] D. Mandal, P. Routh, A.K. Mahato, A.K. Nandi, Electrochemically modified graphite paper as an advanced electrode substrate for supercapacitor application, J. Mater. Chem. A 7 (2019) 17547–17560, https://doi.org/10.1039/c9ta04496e.

[82] K. Yang, K. Cho, S. Kim, Effect of carbon black addition on thermal stability and capacitive performances of supercapacitors, Sci. Rep. 8 (2018) 1–7, https://doi.org/10.1038/s41598-018-30507-5.

[83] N. Bundaleska, J. Henriques, M. Abrashev, A.M.Botelho do Rego, A.M. Ferraria, A. Almeida, F.M. Dias, E. Valcheva, B. Arnaudov, K.K. Upadhyay, M.F. Montemor, E. Tatarova, Large-scale synthesis of free-standing N-doped graphene using microwave plasma, Sci. Rep. 8 (2018) 1–11, https://doi.org/10.1038/s41598-018-30870-3.

[84] P. Tamilarasan, S. Ramaprabhu, Ionic liquid-functionalized partially exfoliated multiwalled carbon nanotubes for high-performance supercapacitors, J. Mater. Chem. A 2 (2014) 14054–14063, https://doi.org/10.1039/c4ta02718c.

[85] M. Ciszewski, A. Mianowski, G. Nawrat, P. Szatkowski, Reduced graphene oxide supported antimony species for high-performance supercapacitor electrodes, ISRN Electrochem. 2014 (2014) 1–7, https://doi.org/10.1155/2014/826832.